Progress In Electromagnetics Research B, Vol. 94, 145–174, 2021

Space and Leaky Wave Radiation from Highly Lossy Biological Cylindrical Human-Limps Models

Xenofon M. Mitsalas[1], Theodoros N. Kaifas[2], and George A. Kyriacou[1, *]

Abstract—The continuous and discrete radiation spectrum of a highly dielectric constant structure with extremely high losses is revisited herein. This work is motivated by the need of efficient electromagnetic power extraction from antenna-sources implanted into the human body. As the dielectric constant of biological tissues varies between 35 and 80 with a conductivity increasing from 0.5 to 2 S/m with frequency, the involved propagation and particularly radiation phenomena cannot be described by the current state of the art published research. Since the scope of the biomedical applications refers to the communication or energy transfer between an implanted device and an external one, the problem to be addressed involves primarily the near field and secondary the far-radiated field. Many of human body parts as the hands, legs, torso, and neck can be modeled as cylinders. Indicatively, a non-magnetic infinite cylinder with an average dielectric constant $\varepsilon_{r1} = 58.1$ and conductivity $\sigma = 1.69$ S/m is considered, with focus on the hand with average radius 2.75 cm. Although a plethora of excellent publications elaborates both analytically and numerically on the radiation from dielectric cylinders including losses, there is not any work studying rods with so high dielectric constants and extremely high losses (loss tangents around unity or higher), while most of them are dealing with the far field rather than near field. Classical works reveal radiation due to the discrete surface and leaky modes as well as a continuous spectrum, while complex modes appearing as quadruplets are found responsible for only energy storage. These are indications of discrete modes transitions as dielectric losses are increased. It is herein proved that indeed increasing losses are causing not only mode transition but also a change in their nature as surface or leaky, while the complex mode quadruplet breaks resulting in radiation in both the near and far fields, while losses have significant effects in the continuous spectrum (sky or space wave). These phenomena are exploited to serve the main purpose of this paper aiming to devise a physical mechanism supporting efficient energy and signal transferring inwards or outwards a highly lossy, high dielectric constant cylinder. The novelty of the proposed methodology stems from a Wiener-Hopf based non-meromorphic Kernel factorization resulting in a field product representation. This is composed of well defined individual terms with each one of them building on a specific pole-mode. The proposed formulation is found to be equivalent to the generalized "multiplicative" and "additive" steepest descent methods regarding the far field evaluation, but additionally is capable of providing the near field as well. The latter feature supports important biomedical applications. Due to the huge extent of the subject and in order to facilitate the continuous spectrum, the analysis is restricted to the excitation by an infinitesimal electric dipole positioned at the origin and oriented along the axis of the cylinder. Studying this structure, a low attenuation low order mode is encountered which is mainly responsible for the energy transferring. This is in accordance with Frezza et al. findings for a "deeply penetrating" mode into highly lossy media.

Received 6 September 2021, Accepted 9 December 2021, Scheduled 23 December 2021

* Corresponding author: George A. Kyriacou (gkyriac@ee.duth.gr).

[1] Microwaves Lab, Department of Electrical and Computer Engineering, Democritus University of Thrace, Xanthi, Greece.

[2] Department of Physics, Aristotle University of Thessaloniki, Greece.

1. INTRODUCTION

Implantable medical devices are becoming an attractive bioengineering trend during the recent years serving important issues of medical treatment and diagnosis, such as preventive and post-surgery monitoring, local stimulation and drug delivery and biomimetic prosthesis [1–3]. Among them, brain and cardiac implants are of critical importance with an emphasis on cardiac pacemakers [4, 5]. To discuss the references' findings, we should note that there are two important issues related to all implanted devices: their wireless-power delivering-charging and their communication link to antennas (transceivers) external to the body [1–5]. Thus, results here indicate that both of them ask for an electromagnetic energy transferring inwards or outwards from the human body. However, the biological tissues environment is too hostile to the required implanted antennas due to their excessively high losses being electrolytes rather than dielectrics. This turns to be almost prohibitive to the transfer-propagation of electromagnetic waves from the interior of the body toward its exterior. The vice-versa electromagnetic waves transfer-propagation is the same as it which stems from the reciprocity theorem. The tissues' conductivity is so high (between 0.7 to 2 S/m), so that implanted antennas could be short circuited by its surrounding media, and for this reason they are covered with silicone. Besides these difficulties, the internal body structure is highly inhomogeneous in both the dielectric constant and conductivity (muscles can be even anisotropic in conductivity), rendering the electromagnetic analysis extremely complicated.

Numerical techniques could serve this task; however, they do not offer any physical insight into how to overcome the encountered difficulties into the electromagnetic wave propagation through these electrolyte-type media. The question to be posed here could be "Is there any type of specific antenna geometry able, ([4–7]), to excite some kind of electromagnetic wave capable of propagating through these biological tissues, so as to carry energy or signal-information outside the human body?" For this question to be addressed simplified models to be analytically studied are inevitable. It was conveniently realized by a number of researchers [5–9] that indeed most human organs as legs, hands, neck, and torso can be modeled as dielectric cylinders. These, to a first order approximation, are considered as infinite dielectric waveguides of very high dielectric constant of the order of 35 to 80 and excessively high conductivity between 0.5 and 2 S/m in the RF and microwave regime. The latter yields a loss tangent of the order of unity or even higher.

Dielectric waveguides are extensively studied in the past but for low dielectric constants and very low loss tangents, mostly lower than about 0.1, since the targeted applications referred to microwave or optical waveguides build for low loss wave propagation. Even though dielectric waveguides are studied for their energy leakage-radiation, non the less the focus is mostly on their far field when being operated as antennas. Their electromagnetic radiation is classified as a continuous spectrum and a discrete spectrum composed of surface and leaky waves [10–12]. As for the planar dielectric waveguides, a quad of complex discrete modes which in the absence of losses, (or for very small losses), are perfectly symmetric in terms of their real, (phase constant), and imaginary, (attenuation constant), parts. This property was exploited to justify their inability for energy transfer [13], based on the Poynting vector.

The problem of highly lossy dielectric waveguides has already attracted the interest of a few researchers as [14–16], which have contributed toward the basic question considered herein but for relatively low losses and small values in the dielectric constant. To discuss their results, we should note that an important observation, made by Kamel and Omar [16], is that increased losses break the perfect symmetry of the quadruplet of complex modes to two symmetric pairs enabling the possibility for them to become radiative. Simultaneously, the surface and leaky wave poles are migrating in the complex plane changing their nature as both become complex and, in some cases, cease to radiate anymore. From an intuitive point of view, the extremely high losses may negate wave propagation in the ordinary-established understanding, since this is related to the wave guidance caused by multiple reflection-diffraction at the dielectric-air interface. The presence of so high losses renders the wave emanating from the source-antenna very weak when it reaches the interface to the air. This point of view leads to the expectation that the energy-leakage radiation is expected to result from waves-rays impinging almost normally to the interface. These rays mainly comprise the continuous spectrum, which have phase constants [17], less than the external media wavenumber, ($\beta_z < k_0$), and thus corresponding to rays impinging at angles smaller than the critical for total reflection (Brewster angle). However, leaky waves are included among these rays, with their only difference that their phase constant fulfills the

dielectric waveguide characteristic equation, namely the condition for constructive interference when undergoing the multiple reflection-diffraction at the dielectric-air interface, which is now questionably sustainable due to high losses. The insight of questionable wave-guidance motivated a few researchers to study the problem as "wave diffraction at the air-highly lossy dielectric interface", usually assumed locally planar as by Frezza et al. [17–20]. Focusing on those results it is readily concluded that a very promising finding of [17–20] is that some leaky waves may deeply penetrate a highly lossy dielectric. This is a strong indication that "there should be a discrete mode either leaky or one of the modified complex pairs that is capable of efficiently carrying energy outwards from the lossy dielectric cylinder (outwards from the human body)". The fact that this should be a discrete mode is based on the observation that this phenomenon occurs for a specific angle, not a spectrum of angles of incidence.

Modes' excitation phenomena and radiation mechanisms in open waveguiding structures have attracted so far considerable research attention. Propagation characteristics of leaky waves are rigorously investigated by Tamir and Oliner in [10–12] where their field distribution and power transport properties are explored in detail. For circular dielectric waveguides, a relative concrete analysis is given by Snyder and Mitchell [21, 22] emphasizing the excited continuous mode spectrum due to the scattering of a plane wave at oblique incidence from a dielectric rod. The optimization of the leaky wave radiation has been elaborated by Jackson et al. [23–25] deriving general rules based on the dispersion characteristic of the involved leaky waves that allow to obtain maximum power density at the desired direction. Furthermore, with a focus on surface modes, the problem of their excitation and far field evaluation was rigorously investigated using Green's functions' method by Wait [26], providing a complete solution for the general problem of a plane wave incident obliquely on a cylinder of infinite length. Methods regarding predictions on the placement of poles on k_z-domain, in cylindrical dielectric structures, were rigorously established by Snitzer [27]. Therein [27], the cut-off conditions of both axially symmetric and hybrid modes are established, and the eigen-field of the lower order modes is evaluated near the cut-off frequencies as well as far from them. Characteristics of propagation modes are also discussed there [27], but the problem is characterized by the absence of material losses. In the analysis of the field of open-waveguides, a very interesting orthogonal expansion technique in systems of proper and improper modes was proposed in [28–30]. In [28–30], the ortho-normalizing factors of improper modes revealed a strong correlation of the latter to space wave. In the work of Singh et al. [31], on a lossless dielectric circular cylindrical rod, the strong correlation of the scanning beam characteristics to rod's parameters, (medium's dielectric constant and cylinder radius), was demonstrated. Shigesawa and Tsuji [14] were the first who introduced and examined the effects of dielectric losses, for planar lossy structures, on the placement of leaky poles in the complex domain, (leaky spectral gap under losses). Pole trajectories, although only cases of absence or low losses were considered, were the primary concern of the works of Ufimtsev et al. [32]. On a similar direction, Neve and Paknys [15] focused on poles' locations and trajectories with the presence of losses in planar dielectric structures. These works indicate that when frequency and/or the other electrical parameters, (permeability, dielectric constant and its loss tangent), of the structure vary, the poles' positions, normalized phase, and attenuation constants change respectively forming clear paths, (trajectory curves), on the complex wavenumber plane. Those pole trajectories have definite effects on the way the respective structure radiates. In order to tackle those complex phenomena, we contribute here the Space Wave Product Representation which stems from the product factorization of non-meromorphic functions. Accordingly in our study, the, (near or far), field expression is written as a product of well-defined individual terms with each depending on a single specific pole/mode. Subsequently, the product representation produces the respective sum formula which is the one utilized to provide understanding over the related phenomena.

The paper is organized as follows. In Section 2, the problem statement is given, and our contribution for the Field Product Representation is presented. In Section 3, the paths of the modes' solution in the complex plane are investigated. In Section 4, we focus on the radiated field. Explicitly, the studied models refer to the *human-arm cylinder model*. In this model, a cylinder of radius 2.75 cm, a real part of relative permittivity of $\varepsilon'_{r1} = 58.1$, relative permeability of 1, and a conductivity of 1.69 [S/m] is used [6]. For this purpose, two operating frequencies $f = 1.6$ and 0.4 GHz are used. The first is referred as optimum frequency for energy transfer in body area networks by Poon et al. [1–3]. The 400 MHz belongs to a band of resonant frequencies as noted in the IEEE Standards 802.15.6TM-2012 [33, Ch. 4], of low frequency zone dealing with human exposure. The imaginary part of material's

relative permittivity is defined as $\varepsilon''_{r1} = \sigma/\omega\epsilon_0$ [34, p. 13]. So, the first, (1.6 GHz), operating frequency responds to $\varepsilon_{r1} = 58.1 - j19$, and the second, (0.4 GHz), to $\varepsilon_{r1} = 58.1 - j76$. Trajectories of the leaky poles as both parts, (real and imaginary), of medium's complex relative permittivity increase, reveal the variation of their radiation behavior.

2. PROBLEM STATEMENT AND CONTRIBUTION TO SPACE WAVE EVALUATION

2.1. Problem Statement

A homogeneous circular cylindrical rod, (Region-1), of complex relative permittivity ε_{r1}, ($\varepsilon_1 = \varepsilon_0\varepsilon_{r1}$) and radius α, immersed in free space, (Region-2), and aligned along the z-axis, is considered, (as shown in Fig. 1). The field at a point ρ, φ, z, (in cylindrical coordinates or equivalently at r, φ, θ expressed in spherical ones), outside the rod, is given as linear expansion, of eigen-solutions, $e^{-jm\varphi}H_m^{(2)}(k_\rho\rho)e^{-jk_z z}$ in [35, 36]. Note that m denotes the azimuthal index; k_z, (k_ρ), is the longitudinal, (transverse), wavenumber; and $H_m^{(2)}(\cdot)$ is the m-th order Hankel function of the second kind. A time convention of $e^{+j\omega t}$ is adopted. For an infinitesimal, z-directed, electrical current density dipole, acting as a source and placed at (ρ', φ', z'), the field in the air region-2 of Figs. 1(a)–(b) obeys the following equation [35, Sec. 3] or [36]:

$$\begin{bmatrix} E_z \\ H_z \end{bmatrix} = \frac{-j}{4\pi\omega\varepsilon_1} \sum_{m=-\infty}^{+\infty} e^{-jm(\varphi-\varphi')} \int_{-\infty}^{+\infty} dk_z e^{-jk_z(z-z')} H_m^{(2)}(k_{\rho 2}\rho) \begin{bmatrix} G_1^{(m)}(k_z;\rho,\rho') \\ G_2^{(m)}(k_z;\rho,\rho') \end{bmatrix} \tag{1}$$

where $\mathbf{G}_{1,2}^{(m)}(k_z;\rho,\rho')$, (multiplied by $H_m^{(2)}(k_{\rho 2}\rho)$), is the so-called Spectral Domain Green's function determined by the boundary conditions for the two regions of Fig. 1 [35, Sec. 3].

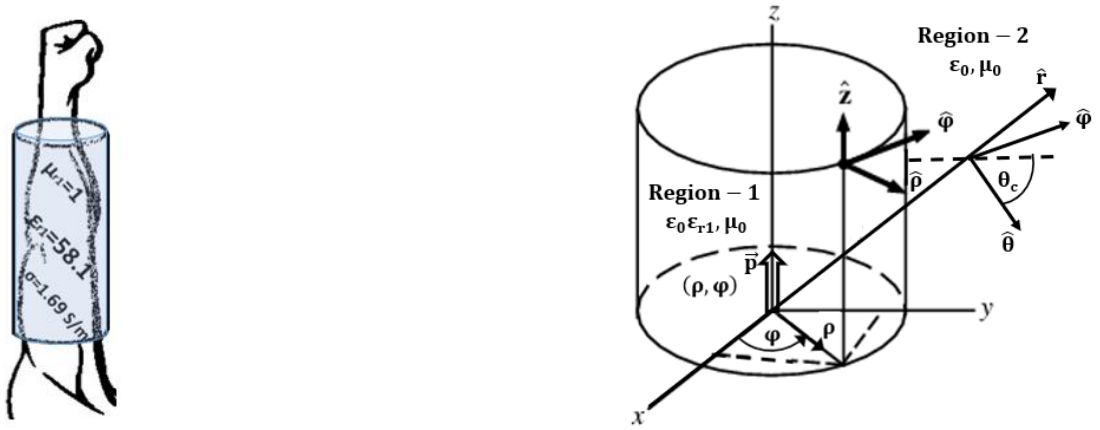

Figure 1. The structure under study: (a) A human hand modeled by a highly lossy dielectric cylinder, (b) an open dielectric waveguide excited by a centrally located infinitesimal electric dipole source.

In Eq. (1), the integration is carried out following the Sommerfeld Integration Path, (SIP). Since direct integration of Eq. (1) along the SIP involves major challenges, often the Cauchy theorem is employed to integrate in the complex k_z plane. In this case however, one has to take into account the diverse k_z plane terrain. Indeed, it is well known that the complex k_z plane is assembled by two Riemann sheets, (due to the ambiguity of the sign definition of the transverse wavenumber, $k_{\rho 2} = \pm j\sqrt{k_z^2 - k_0^2}$). Each sheet is assembled by four quadrants, T_1, T_2, T_3, T_4 for the top, (imaginary ($k_{\rho 2}$) < 0), and B_1, B_2, B_3, B_4 for the bottom, (imaginary ($k_{\rho 2}$) > 0), Riemann sheet, respectively, (in both cases counting the quadrants counterclockwise) [37]. Furthermore, the k_z terrain hosts branch cuts, (formed

by continuum of poles since the structure under study is open) [38, Ch. 5], and numerous discrete poles that are distributed on the four plus four quadrants. Thus, the Cauchy complex integration, alternative to the SIP, is not free of problems since poles should be found, and the integral around the branch cut is to be evaluated.

Usually, the space wave estimation can be tackled by representing, (after expressing the integral around branch cut from the longitudinal, k_z, to transverse, k_ρ, wavenumber), the integral to a transformed domain where the branch cut is alleviated. Indeed, utilizing [38, Sec. 5.3c], $k_z = k_0 \sin u$, (with k_0 being the free space wavenumber), the k_z wavenumber plane is transformed to a respective complex angular $u = u_R + ju_I$ wavenumber plane. All quadrants in top and bottom Riemann sheets are mapped in their equivalent domains-strips in the single-sheeted complex angular plane, (as it is shown for example in [38, Fig. 5.3.4a]). This is the steepest descent plane where the steepest descent path, (SDP), method of integration is usually employed [38, Fig. 5.3.4]. For the near field, one usually needs to numerically compute the integral at each observation point ρ, φ, z (or r, φ, θ in the spherical coordinates). Fortunately, for the far-field computation, ($k_0 r \gg 1$), closed form expressions are available since the integral gets significant contribution only from the integration path near the saddle point. Admittedly, there are variations of the related techniques ranging from nonuniform [38] to uniform [38, 39], asymptotic evaluation of the integral. In any case, the steepest descent method results in the evaluation of the far-field, (space-wave radiation). Specifically, the m-th term of Equation (1) is given in the form [31], ($Z_0 = 120\pi$ [Ω], the free-space impedance):

$$E_\phi^{(m)} = \frac{-2\omega\mu_2}{k_{\rho 2}} j^{m+1} \left. G_2^{(m)} \right|_{k_z = k_o \sin(\theta_c)} \frac{e^{-jk_2 r}}{r} \quad \text{and} \quad H_\theta^{(m)} = -E_\phi^{(m)}/Z_o \tag{2}$$

$$H_\phi^{(m)} = \frac{-2\omega\varepsilon_2}{k_{\rho 2}} j^{m+1} \left. G_2^{(m)} \right|_{k_z = k_o \sin(\theta_c)} \frac{e^{-jk_2 r}}{r} \quad \text{and} \quad E_\theta^{(m)} = +Z_o H_\phi^{(m)} \tag{3}$$

where $k_{\rho i} = \sqrt{k_i^2 - k_z^2}$, $i = 1, 2$, $k_1 = k_0\sqrt{\varepsilon_{r1}}$, and $k_2 = k_0$ while the normalized (to k_0) radial wavenumbers are denoted as $\overline{k}_{\rho 1} = \sqrt{\varepsilon_{r1} - (k_z/k_0)^2}$ and $\overline{k}_{\rho 2} = \sqrt{1 - (k_z/k_0)^2}$. Since the dipole is placed at the cylindrical rod's origin, (Fig. 1), the radiated electric field of Eq. (2) exhibits only an E_θ far-field component resulting from the $m = 0$ term due to the axial symmetry [31, Eq. (15)] or [35]:

$$E_\theta = E_\theta^{(0)} = g(a) F(k_z) \frac{e^{-jk_2 r}}{r} \quad \text{with} \quad g(a) = \frac{-\sqrt{\varepsilon_2\mu_2}k_0}{2\pi^2 a} \tag{4}$$

$$F(k_z) = \frac{k_{\rho 1}/k_0}{\varepsilon_1 k_{\rho 2} J_1(k_{\rho 1}a) H_0^{(2)}(k_{\rho 2}a) - \varepsilon_2 k_{\rho 1} J_0(k_{\rho 1}a) H_1^{(2)}(k_{\rho 2}a)} = \frac{\overline{k}_{\rho 1}}{D(k_z)} \tag{5}$$

The denominator $D(k_z)$ of the function $F(\lambda)$ comprises the characteristic equation of the cylindrical waveguide $D(k_{zp}) = 0$ which can be solved for the propagation constants k_{zp}.

2.2. Alternative Evaluation of Near and Far Field

The present theoretical contribution exploits an alternative evaluation of the field that extremely augments intuition and builds on the concept of leaky wave radiation. In the expressions that follow, k_z is denoted as λ. Herein, the observation angle θ_c, (complementary of angle θ as in Fig. 1(b)), is defined over the cylinder's interface, normal to the z-axis. The proposed approach stems from the function-Kernel factorization that is well established in Wiener-Hopf techniques. Usually, even functions $F(\lambda)$ are factorized into a product of one analytic in the upper λ-half plane $F_+(\lambda)$ and one analytic in the lower λ-half plane $F_-(\lambda)$ as $F(\lambda) = F_+(\lambda)F_-(\lambda)$, where for even functions $F_-(\lambda) = F_+(-\lambda)$ [40–43]. The employed approach was developed for non-even functions by Fikioris et al. [44], appearing in ferrite loaded structures and recently exploited for magnetized plasma loaded structures in our previous work [45]. For the function-kernel $F(\lambda)$ defined in Eq. (5) the factorization is carried out in Appendix A

and reads:

$$\frac{F(\lambda)}{F(0)} = \overbrace{\exp\left[\frac{1}{2\pi j}\left[\int\limits_{\text{C-branch}}\left[\ln\left(1+\frac{\lambda}{x}\right)-\frac{\lambda}{x}\right]\frac{F'(x)}{F(x)}\,dx+\int\limits_{\text{C-branch}}\left[\ln\left(1-\frac{\lambda}{x}\right)+\frac{\lambda}{x}\right]\frac{F'(x)}{F(x)}\,dx\right]\right]}^{F^{\text{branches}}} \cdot \frac{\prod\limits_{n=1}^{+\infty}\left(1+\frac{\lambda}{k_{zn}}\right)}{\prod\limits_{p=1}^{+\infty}\left(1+\frac{\lambda}{k_{zp}}\right)} \tag{6}$$

where:

$$F(0)=\frac{1}{k_0\varepsilon_0}\left[\sqrt{\varepsilon_{r1}}J_1\left(k_0a\sqrt{\varepsilon_{r1}}\right)H_0^{(2)}\left(k_0a\right)-J_0\left(k_0a\sqrt{\varepsilon_{r1}}\right)H_1^{(2)}\left(k_0a\right)\right]^{-1} \tag{7}$$

The exponential factor in Eq. (6) comprises the usual branch-cut integrals, and their integration path goes around the branch-cut as in [40, Fig. A-2 (p. 94)]. The infinite product in the numerator accounts for the zeros k_{zn}, while that of denominator collects the poles k_{zp} contribution of the function $F(\lambda)$. For the convenience of its numerical evaluation, Equation (6) is reformulated in terms of the "positive" and "negative" complex functions $q_+(\lambda)$ and $q_-(\lambda)$, as in Appendix B. Additionally, as poles of even function appear in pairs, $(\pm k_{zp})$, exhibiting an even symmetry, their residues will be of equal values and can be accounted in pairs modifying the infinite product in the denominator of Eq. (6) to take the following form:

$$E_\theta = g(a)\cdot\left[F(0)\overbrace{\left[1-\left(\frac{\lambda}{k_0}\right)^2\right]^{1/2}\cdot e^{q_+(\lambda)+q_-(\lambda)}}^{F^{\text{branches}}}\frac{\prod_n\left(1+\frac{\lambda}{k_{zn}}\right)}{\prod_p\left(1-\frac{\lambda^2}{k_{zp}^2}\right)}\right]\frac{e^{-jk_2r}}{r} \tag{8}$$

$q_\pm(\lambda)$ along with $(1-(\lambda/k_0)^2)^{1/2}$ denote the contribution from the branches, which are defined analytically in Appendix B. The infinite product in Eq. (8) can also be expressed as the sum of residues $L(k_{zp})$, for each pole k_{zp} according to [39, 46]. Thus, Eq. (8) reads:

$$E_\theta = g(a)\cdot F(0)\cdot\left[1-\left(\frac{\lambda}{k_0}\right)^2\right]^{1/2}\cdot e^{q_+(\lambda)+q_-(\lambda)}\cdot\prod\nolimits_n\left(1+\frac{\lambda}{k_{zn}}\right)\cdot\sum\nolimits_p\frac{2\cdot L\left(k_{zp}\right)}{\left(1-\frac{\lambda^2}{k_{zp}^2}\right)}\frac{e^{-jk_2r}}{r} \tag{9}$$

where $L(k_{zp})$ denotes the residue of k_{zp} pole as $\lim\limits_{k_z\to k_{zp}}(k_z-k_{zp})F$. Each pole's contribution is encountered in the field of Eq. (9), via the following expression (10). A similar expression was also obtained by Collin and Zucker [10, Part II, Ch. 20] or Ostner et al. [25] or Singh et al. [31].

$$F_p(\lambda)=\sum\nolimits_p\frac{2\cdot L\left(k_{zp}\right)\bar{k}_{\rho1}}{\left(1-\frac{\lambda^2}{k_{zp}^2}\right)}\left[1-\left(\frac{\lambda}{k_0}\right)^2\right]^{1/2}\Rightarrow F_p(k_0\sin\theta_c)=\sum\nolimits_p\frac{2\cdot L\left(k_{zp}\right)\left[\varepsilon_{r1}-(\sin\theta_c)^2\right]^{1/2}}{\left(1-\frac{(k_0\sin\theta_c)^2}{k_{zp}^2}\right)}\cos\theta_c \tag{10}$$

However, herein the contribution from zeros of the normalized $\bar{k}_{\rho1}=k_{\rho1}/k_0$ of the numerator of Eq. (4) is also encountered in Eq. (10). The poles k_{zp} involved in Eq. (10) can be estimated by solving Eq. (5). In order to track the poles' trajectories, especially near cut-off, Eq. (5) needs to be solved numerically or analytically. Roots can be extracted numerically by solving Eq. (5) via Davidenkos technique [47, 48]. Toward this direction, the work of Yang and Song [49] provides useful methods in order to derive initial guesses in the vicinity of cut-off frequencies.

2.3. Comparison against Established Techniques

The novel closed form field expressions obtained in Equations (6) and (8)–(9) must be validated against already established techniques in terms of formulas and numerical results. For this purpose, the established radiated field evaluation techniques are first summarized. From a first view it seems that the formulas obtained herein Eqs. (8) to (9) share the same form as the multiplicative method proposed in [46, 50, 51]. Following the asymptotic evaluation methodology of [38], the integral Equation (C1) of Appendix C representing the field can be transformed into the strip-domains, and the integration path is deformed to a steepest descent path (SDP). According to [38] the total field is comprised from the SDP integral corresponding to the continuous spectrum and the discrete spectrum resulting from the residue contribution of poles captured-enclosed between SDP and the original integration path (SIP) as in Fig. 2 in the form:

$$\begin{aligned} E_\theta &= -2\pi j \sum \text{Res} \cdot H\left(\theta_c - u_p\right) + \int\limits_{\text{C-SDP}} \widetilde{E}_\theta\left(\lambda\right) e^{-j\lambda z} e^{-j\sqrt{k_0^2-\lambda^2}\rho} d\lambda \\ &= -2\pi j \sum \text{Res} \cdot H\left(\theta_c - u_p\right) + g\left(\alpha\right)/rF\left(k_0 \sin\theta_c\right) e^{-j\left(k_0 r - \frac{\pi}{4}\right)} \end{aligned} \tag{11}$$

where $H(\theta_c - u_p)$ is the Heaviside step function, and θ_c is the saddle point defined by:

$$\cos\left(u_R - \theta_c\right) \cdot \cosh\left(u_I\right) = 1 \tag{12a}$$

via the SDP transform:

$$k_z = k_0 \sin u \tag{12b}$$

with $u = u_R + j u_I$ or $k_z/k_0 = \beta_z - j\alpha_z = \sin u_R \cosh u_I + j \cos u_R \sin h u_I$.

In the first term of the residues' sum in Eq. (11), only the captured poles from SDP are involved. The function $F(\cdot)$ is already defined in Eq. (4). Applying the saddle point method, where the observation angle $u = \theta_c$ in Eq. (11), yields the space wave (second term of Eq. (11)). It is important to recall that as noted by Senior and Volakis [50, p. 33] as well as in [39, 46, 51] formulas (11) are valid when θ_c is a first order Saddle point (true herein), and function $F(k_0 \sin\theta)$ is slowly varying in its vicinity as well as that $F(k_0 \sin\theta)$ to be free of poles near the SDP path. However, the main purpose of the present effect is to evaluate the radiated field of a cylindrical rod when its losses are increased to very high degree as they occur in biological media. It will be proved in the next section that increasing the rod losses causes the poles to migrate reaching or even crossing the SDP path. Hence, it is inevitable to employ a methodology which accounts for poles near the SDP path or close to the saddle point θ_c. It is even preferably to utilize a method accounting for poles contributions through an appropriate weighting factor, wherever their position is. According to Rojas [39], two appropriate methods, a "multiplicative" (Pauli-Clemmow) and an "additive" (Van der Waerden) which are asymptotically the same (term by term) can handle multiple poles lying anywhere in the complex plane, while they can cross the SDP path anywhere or even close to the saddle point. These involve a transition function introduced by Kouyoumjian and Rojas [39]. As concluded in [39] these two methods constitute a generalization in the classical SDP method in Eq. (11) of Felsen and Marcuvitz [38]. In the special case when the poles are far from the saddle point, the transition function tends to unity, and the general expressions can be replaced by an asymptotic expansion which is the same as that of [38]. The multiplicative method was first proposed by Gennarelli and Palumbo [46], later validated by Rojas [39] and summarized by Senior and Volakis [50]. The multiplicative method for the case elaborated herein reads:

$$E_\theta = \pm 2j\sqrt{k_0 r b_p^2}\, e^{k_0 r f(\theta_c)} k_0 \sqrt{\frac{-2\pi}{k_0 r f''\left(\theta_c\right)}}\, F\left(k_0 \sin\theta_c\right) F_C\left(\pm\sqrt{k_0 r b_p^2}\right) \tag{13a}$$

$$f(\theta_c) = -j\cos(\theta_c - u_p) \quad \text{and} \quad b_p^2 = j\left(f(\theta_c) - f(u_p)\right) \tag{13b}$$

$$F_{KP}\left(z^2\right) = 2jze^{jz^2} \int_z^\infty e^{-j\tau^2} d\tau \quad \text{and} \quad F_{KP}\left(z^2\right) = \pm 2jz F_C\left(\pm z\right) \tag{13c}$$

where F_{KP} denotes the Kouyoumjian-Pathak transition function, while F_C is the Clemmow transition function. For the Clemmow transition function in Eq. (13a), there is a sign interchange from "minus" if the pole is captured when $-\frac{3\pi}{4} < \arg(z) < \frac{\pi}{4}$ to "plus", if the pole is captured when

$\frac{\pi}{4} < \arg(z) < \frac{5\pi}{4}$ [50, p. 333–334]. The equivalent "additive" method was originally developed by Van der Waerden [50, p. 334], and it was later generalized by Volakis and Herman [51] and summarized in [50, p. 335]. Applying this method to the present case, the radiated field reads:

$$E_\theta = e^{k_0 r f(\theta_c)} \sqrt{\frac{\pi}{k_0 r}} \sum \frac{\text{Res}}{\mu_p} \left[1 - F_{KP}\left(k_0 r b_p^2\right)\right] + \sqrt{\frac{-2\pi}{k_0 r f''(\theta_c)}}\, e^{k_0 r f(\theta_c)} k_0 F\left(k_0 \sin\theta_c\right) \tag{14a}$$

$$\mu_p^2 = f(\theta_c) - f(u_p) \tag{14b}$$

Both the multiplicative Eq. (13) and the additive method Eq. (14) involve the transition function $F_{KP}(z_p^2)$; $z_p^2 = k_0 r b_p^2$. This function is defined in terms of the standard error function as in Eq. (13c) [52, Ch. 7], and accounts for the proximity of a pole u_p relative to the saddle point θ_c as in Eq. (16d). F_{KP} is explicitly defined in [50, 53], wherein they prove that when its argument is increased beyond $z_p^2 \geq 2$, $F_{KP} \to 1$. Hence, when this tends to unity, a pole (u_p) is away from the saddle point so that $z_p^2 > 2$, then its effect on the SDP integral is negligible, and expressions (13) and (14) are reduced to the classical SDP given in Eq. (11). The same is expected for formulas (8)–(9) proposed herein.

Let us now compare the expression resulting from the Wiener-Hopf factorization in Eqs. (8) to (9) to the "multiplicative" Eq. (13a) and additive Eq. (14a) in a term-by-term approach as done by Rojas [39]. First, the poles residue contributions are the same in the three cases. The branch cut integral herein is defined in Equation (5), and it appears as an argument of an exponential function. The important observation is that the integrand does not involve any oscillating terms, but on the contrary the Kernel function $F'(x)/F(x)$ is multiplied by a logarithmic term. This exhibits logarithmic singularities of $x = \pm\lambda$ and $x = 0$, which can be handled by established techniques during numerical integration. It is important to notify that this integral, denoted as $F_p(\lambda)$ in Eqs. (8) to (9) multiplies the poles residue contribution acting as a weighting factor accounting for their relative position with respect to the integration path. However, the same role is played by the transition function F_{KP} in the two equivalent multiplicative [46] and additive formulas [50, 51] formulas (13)–(14). Thus, it seems that $F_{\text{branches}}(\lambda)$ encapsulates the action of the transition function along with the branch-cut integral, but in the λ-domain. Although this is cumbersome as a numerical integration is prerequisite, it offers the possibility to evaluate both the near and far fields. On the contrary, the multiplicative and additive expansions are directly developed as asymptotic approximations, thus they can only estimate the far field. The latter is adequate for most traditional electromagnetic problems, but not for the case of wearable antennas, or antennas implanted in biological tissues. In the present case what is of primary importance is the evaluation of the field just outside the biological object (cylinder herein) or in its close vicinity. Due to the extremely high losses involved, only this type of near field is expected to be possibly exploited for transferring information or energy inwards or outwards from the human body.

3. MODES-POLES SUPPORTED BY HIGHLY LOSSY DIELECTRIC CYLINDERS

Different parts of the human body can be modeled adequately as biological cylinders: arms, legs, torso, and neck. Although these are cylinders of finite length, important conclusions regarding electromagnetic signals and energy transferring inwards and outwards can be extracted considering infinite cylinders for mathematical convenience. Once a physical insight is acquired, the resulting expressions can be extended to finite cylinders as resonators made from a section of the corresponding waveguide. Herein, an infinite cylinder representing the human arm is considered with a radius 2.75 cm and complex dielectric constant (including the conductivity) of $\varepsilon_{r1} = \varepsilon'_{r1} - j\varepsilon''_{r1} = 58.1 - j76$ and $\varepsilon_{r1} = \varepsilon'_{r1} - j\varepsilon''_{r1} = 58.1 - j19$ at frequencies 400 and 1600 MHz respectively following the Drude model [6]. In order to study the involved mode-pole migration phenomena, the real part $\varepsilon'_{r1} = 58.1$ is kept constant, while the imaginary part is varied as $\varepsilon''_{r1} = 0$ to 76. The study starts with the modes-poles' estimation and their migration. Then, it is extended to the radiation regarding both the near and far fields.

3.1. Poles Migration due to Increased Losses

The modes of the dielectric rod can be estimated by the roots of the characteristic equation $D_0(k_z) = 0$, which constitutes the denominator of Eq. (4). This corresponds to the special case of axially symmetric

modes ($m = 0$), while the general form for arbitrary azimuthal index m can be written as (Appendix C):

$$D_m^{-1} = s^2y^2 \cdot \begin{bmatrix} sy \begin{pmatrix} j\omega\mu_1 J'_m(s) H_m^{(2)}(y) y \\ -j\omega\mu_2 H_m^{'(2)}(y) J_m(s) s \end{pmatrix} & -mk_z \begin{pmatrix} J_m(s) H_m^{(2)}(y) y^2 - \\ H_m^{(2)}(y) J_m(s) s^2 \end{pmatrix} \\ -mk_z \begin{pmatrix} J_m(s) H_m^{(2)}(y) y^2 - \\ H_m^{(2)}(y) J_m(s) s^2 \end{pmatrix} & sy \begin{pmatrix} j\omega\epsilon_1 J'_m(s) H_m^{(2)}(y) y \\ -j\omega\epsilon_2 H_m^{'(2)}(y) J_m(s) s \end{pmatrix} \end{bmatrix}$$
$$\cdot \left[-s^2y^2 \begin{pmatrix} j\omega\epsilon_1 J'_m(s) H_m^{(2)}(y) y \\ -j\omega\epsilon_2 H_m^{'(2)}(y) J_m(s) s \end{pmatrix} \begin{pmatrix} j\omega\mu_1 J'_m(s) H_m^{(2)}(y) y \\ -j\omega\mu_2 H_m^{'(2)}(y) J_m(s) s \end{pmatrix} \right.$$
$$\left. + (mk_z)^2 \begin{pmatrix} J_m(s) H_m^{(2)}(y) y^2 - \\ H_m^{(2)}(y) J_m(s) s^2 \end{pmatrix}^2 \right]^{-1} \tag{15}$$

where the arguments of Bessel and Hankel functions are denoted as $s = k_{\rho 1}\alpha$ and $y = k_{\rho 2}\alpha$, respectively. The dielectric rod is studied for two different frequencies of 0.4 and 1.6 GHz and three different levels of losses:

(i) Lossless: 400 MHz ($\varepsilon'_{r1} = 58.1$, $\varepsilon''_{r1} = 0$), 1600 MHz ($\varepsilon'_{r1} = 58.1$, $\varepsilon''_{r1} = 0$)

(ii) Moderate Losses: 400 MHz ($\varepsilon'_{r1} = 58.1$, $\varepsilon''_{r1} = 35$), 1600 MHz ($\varepsilon'_{r1} = 58.1$, $\varepsilon''_{r1} = 8$)

(iii) High Losses: 400 MHz ($\varepsilon'_{r1} = 58.1$, $\varepsilon''_{r1} = 76$ or $\tan\delta = 1.31$), 1600 MHz ($\varepsilon'_{r1} = 58.1$, $\varepsilon''_{r1} = 19$ or $\tan\delta = 0.33$).

The characteristic equation is solved using the Davidenko' technique [47, 48]. Three types of modes are expected, surface waves, leaky waves, and complex improper modes. The results for the axially symmetric case are presented in Figs. 2–3, and they can be discriminated into surface and leaky waves. In order to get an insight into the migration when losses (ε''_{r1}) are increased, these roots are transferred to the complex steepest descent domain where the branch cut $\mathrm{Re}(k_{\rho 2}) = 0$ of $k_{\rho 2} = (k_0^2 - \lambda^2)^{1/2}$ is removed through the transformation $u_p = u_R + ju_I$ and $k_z/k_0 = \sin u_p = \beta_z - j\alpha_z = \sin u_R \cosh u_I + j \cos u_R \sin hu_I$. Modes are evaluated as roots of the characteristic equation $D(k_{zp}) = 0$ defined in Eq. (5), and consequently their positions are plotted at both operating frequencies (400 MHz and 1600 MHz) in the k_z and $k_{\rho 2}$ planes (Figs. 2(c)–(d) and Figs. 3(c)–(d)), as well as in the complex angle (SDP) plane domain (Figs. 2(a)–(b) and Figs. 3(a)–(b)) via the SDP transform of Eq. (12b). The horizontal and vertical axes in Figs. 2(a)–(b) (for 400 MHz) and Figs. 3(a)–(b) (for 1600 MHz) denote the real and imaginary parts of the complex angle u_p, respectively. Extreme steepest descent paths which determine the upper and lower limits of the captured region in complex angle plane are indicated as Upper Steepest Descent Path (USDP) and Lower Steepest Descent Path (LSDP) in Figs. 2(a)–(b) and 3(a)–(b), and their contour is evaluated by setting $\theta_c = \pi/2$ in Eq. (12a) for USDP and $\theta_c = -\pi/2$ for LSDP. Light dashed lines in Figs. 2(a)–(b) and 3(a)–(b) denote the original Sommerfeld Integral path (SIP). The improper leaky mode with the minimal axial attenuation constant α_z is marked with the letter A in Figs. 2–3. In the $k_{\rho 2}$-plane, quadrants with $\mathrm{Im}(k_{\rho 2}) > 0$ belong to the improper (bottom) Riemann sheet, while those with $\mathrm{Im}(k_{\rho 2}) < 0$ belong to the proper (top) Riemann sheet. Those quadrants are also deformed in the complex angle plane, via the transform of Eq. (12b) and consequently are labeled as B (for Bottom Riemann Sheet) and T (for Top Riemann Sheet) in Figs. 2–3 similar to [37, 39].

Improper poles in Figs. 2–3 are depicted with filled markers and proper poles with empty markers. It is important to observe that for this axially symmetric $m = 0$ case TM^z_{0n} or TE^z_{0n}, the complex quadruplet of mode is absent. Although this work is focused on $m = 0$ case, the next group of hybrid modes HE^z_{1n} or EH^z_{1n} are estimated and presented in Subsection 3.4. It is then observed that indeed a quadruplet of complex hybrid modes exists. As expected, when losses are increased the imaginary part of both k_z and $k_{\rho 2}$ becomes higher, (Figs. 2(c)–(d)), while in the transformed domain the poles move away from the real axis, (u_R), deeper into the strips or larger imaginary part, (u_I), as in Figs. 2(a)–(b). Similar phenomena are observed at both frequencies of 400 MHz and 1600 MHz as denoted in Figs. 2 and 3. The main question here is whether increasing losses causes a change in the nature of a pole making that to alter its contribution to radiated near or far field as well as regarding its maximum

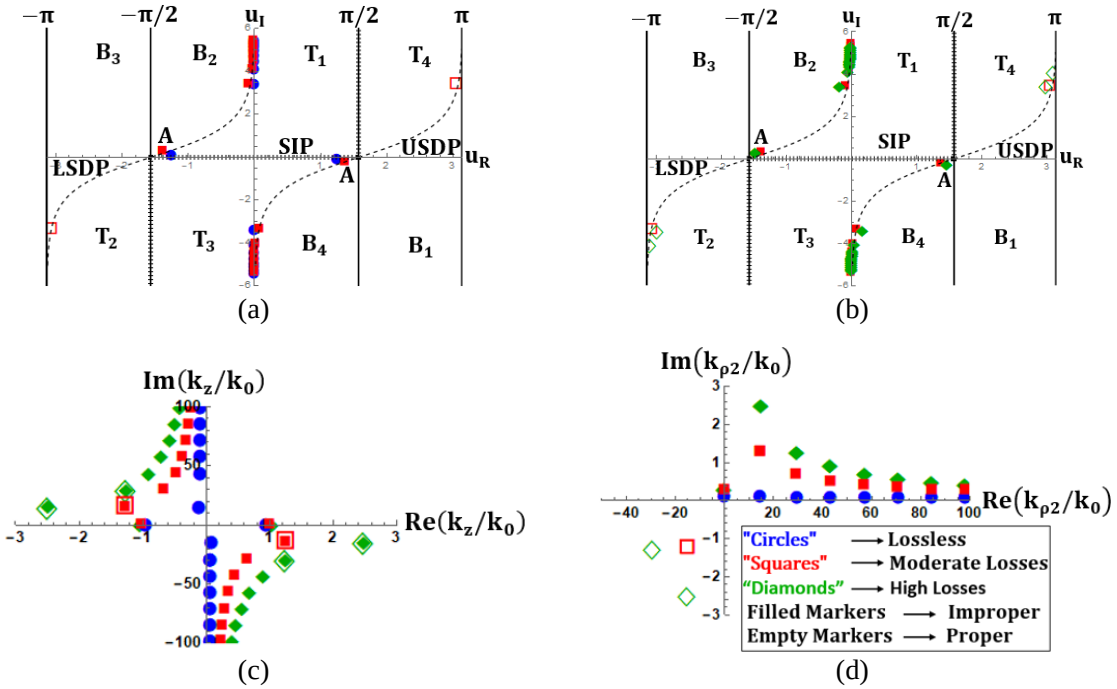

Figure 2. TM^z_{0n} poles' positions at 400 MHz: (a) lossless (blue)-moderate losses (red) comparison on SDP plane, (b) moderate losses (red)-high losses (green), on SDP plane, (c) k_z-plane, (d) $k_{\rho 2}$ plane. Quadrants T_1–T_4 and B_1–B_4 numbering follows [37, p. 12]. Common index in the last figure.

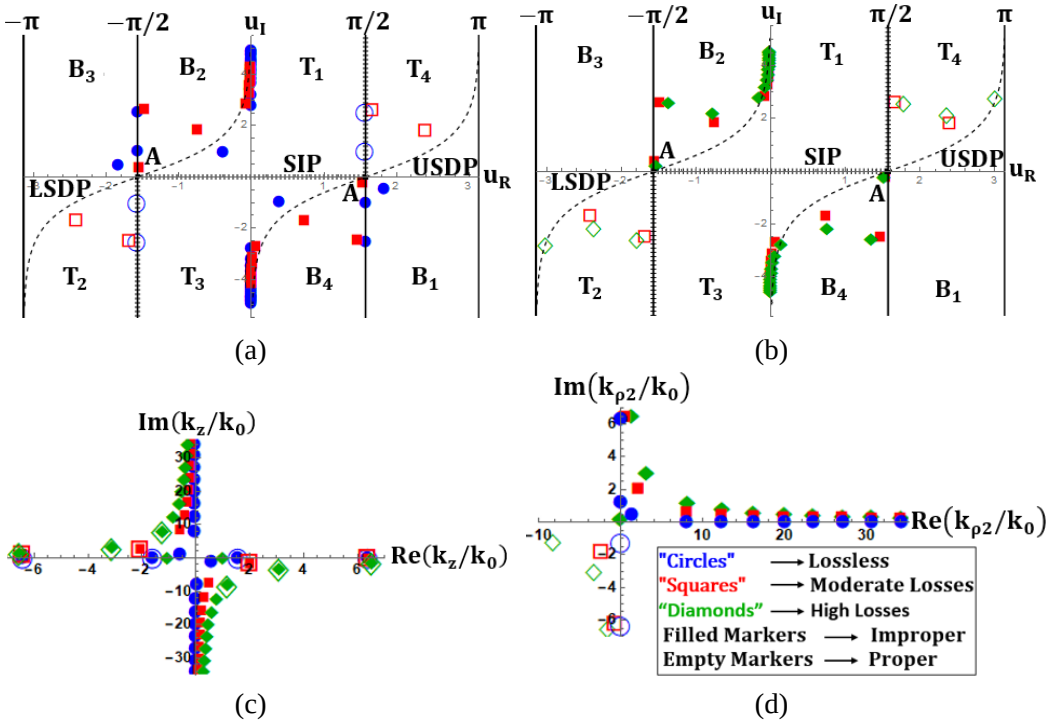

Figure 3. TM^z_{0n} poles' positions at 1600 MHz: (a) lossless (blue)-moderate losses(red) comparison on SDP plane, (b) moderate losses (red)-high losses (green), on SDP plane, (c) k_z-plane, (d) $k_{\rho 2}$ plane. Quadrants T_1–T_4 and B_1–B_4 numbering follows [37, p. 12]. Common index in the last figure.

field angle. A first indication from Figs. 2(a)–(b) or Figs. 3(a)–(b) is that captured poles of the lossless case (blue circles) may move outside the LSDP-USDP area. According to the classical SDP, these poles should cease to contribute to radiation. On the contrary according to [39, 50], these may still have a significant contribution depending on their proximity to the saddle point. Explicit investigation of modes-poles trajectories is discriminated next for three different types: leaky and surface modes, the dominant mode, and quadruplets of complex modes.

3.2. Leaky and Surface Modes

The first five modes supported by the dielectric rod of Fig. 1 are tabulated in Table 1 ordered according to an increasing imaginary part of their propagation constant. This table is restricted to axially symmetric TM_{0n} modes, since only these can be excited by the centrally located dipole source oriented along the z-axis due to its symmetry. A first important observation is that each surface wave mode ($\beta_z/k_0 > 1$) exhibits both a proper branch (located in T_4) and an improper branch (located in B_4) as illustrated in Figs. 2, 3, 4 and depicted in Table 1. This is in accordance to a plethora of publications (e.g., [37, 49]), which prove that surface waves above their cut-off (actually turn-on) may exhibit a bifurcation to a proper and an improper branch. However, the first dominant mode (#1 in Table 1) remains in the improper quadrant B_4, when either its β_z/k_0 is less or greater than 1, because it is not reaching any possible bifurcation point. It will be then proved that this is the dominant leaky mode responsible for the main part of energy leakage (inwards or outwards) from the dielectric rod. Thus, its trajectory will be closely followed versus the increasing losses. Besides that, it is herein realized that this is the mode enabling the deep wave penetration into highly lossy media, which was first observed by Frezza et al. [18–20]. A separate subsection is devoted to this phenomenon due to its high importance. Additionally, it must be noted that the excited modes are not strictly surface or leaky, but they became complex due to high losses. However, they are checked with Hessel's formula [10, Part II, p. 174–181] for leaky modes and found to obey that, providing their maximum contribution to the radiated field (Table 1) toward $u_{pR} = \theta_c$, (θ_c the complementary angle-direction as in Fig. 1), namely when the real part of the pole (u_{pR}) is equal or close to the saddle point.

The pole locations in Figs. 2–3 and Table 1 are depicted for specific losses encountered in the human arm model. It was then decided to track the locus of these modes when losses are increased from zero to

Table 1. TM modes in the arm cylinder at frequencies 1.6 and 0.4 GHz, ordered by increasing attenuation constant in z-direction. Orientation of corresponding modal maximum in radiation pattern is denoted by $\theta_{c,\max}$.

freq	**Character**	**Number**	$\boldsymbol{k_z/k_0}$	$\boldsymbol{k_{\rho 2}/k_0}$	$\boldsymbol{u_R = \theta_{c,\max}}$	$\boldsymbol{u_I}$
1.6 GHz	Improper	#1	$1.0223 - j0.0084$	$0.0398 + j0.2159$	$87.77°$	$-12.28°$
		#2	$6.546 - j1.454$	$1.4704 + j6.4729$	$77.34°$	$-148.45°$
		#3	$3.106 - j3.119$	$3.2 + j3.027$	$44.14°$	$-124.64°$
		#4	$1.209 - j8.073$	$8.1334 + j1.2$	$8.45°$	$-160.22°$
		#5	$0.796 - j12.306$	$12.35 + j0.79$	$3.69°$	$-183.75°$
	Proper	#2	$6.556 - j1.445$	$-1.4613 - j6.4829$	$102.53°$	$148.52°$
		#3	$3.071 - j3.015$	$-3.0975 - j2.9892$	$135.25°$	$123.34°$
		#4	$1.144 - j8.075$	$-8.1355 - j1.1355$	$172°$	$160.17°$
0.4 GHz	Improper	#1	$1.03632 - j0.0292$	$0.1044 + j0.2898$	$84.25°$	$-16.46°$
		#2	$2.582 - j14.975$	$15.0074 + j2.5764$	$9.76°$	$-195.68°$
		#3	$1.323 - j29.477$	$29.4939 + j1.322$	$2.57°$	$-233.66°$
		#4	$0.905 - j43.47$	$43.4815 + j0.9048$	$1.19°$	$-255.86°$
		#5	$0.693 - j57.297$	$57.3057 + j0.6929$	$0.69°$	$-271.67°$
	Proper	#2	$2.491 - j15.035$	$-15.067 - j2.486$	$170.61°$	$195.84°$
		#3	$1.258 - j29.549$	$-29.566 - j1.256$	$177.56°$	$233.79°$

these values as $\varepsilon''_{r1} = 0$ to 76 at 400 MHz and $\varepsilon''_{r1} = 0$ to 19 at 1600 MHz. These trajectories are sought so as to gain an insight on whether their radiation-energy leakage is maximized. As noted above, the energy leakage is maximized toward $u_{Rp} = \theta_c$, and its intensity increases as the pole itself comes closer to θ_c, (close to the saddle point). Since θ_c scans the angles from $-90°$ to $90°$ or u_{Rp} from $-\pi/2 \tau o \pi/2$, then the leakage will be maximized when the pole u_p tends closer to the real axis, $(u_I = 0)$ [10, Part II, Sec. 21]. The resulting poles trajectories versus the increasing losses (ε''_{r1}) are depicted in Fig. 4. It is observed that only the dominant #1 leaky wave mode is close to real axis $(u_I = 0)$. At a specific loss, the dominant mode trajectory crosses the USDP as $\varepsilon''_{r1} = 27$ at 400 MHz, while at 1600 MHz it remains in the whole range of $\varepsilon''_{r1} = 0$ to 19 outside the USDP. Beyond that point, the pole is not captured between the LSDP and USDP (shaded in Fig. 4(a)) in the classical mean. However, it is expected to contribute to radiation as discussed in Section 2.3. Regarding the higher order modes, some of them remain captured, while others are driven outside the LSDP-USDP area.

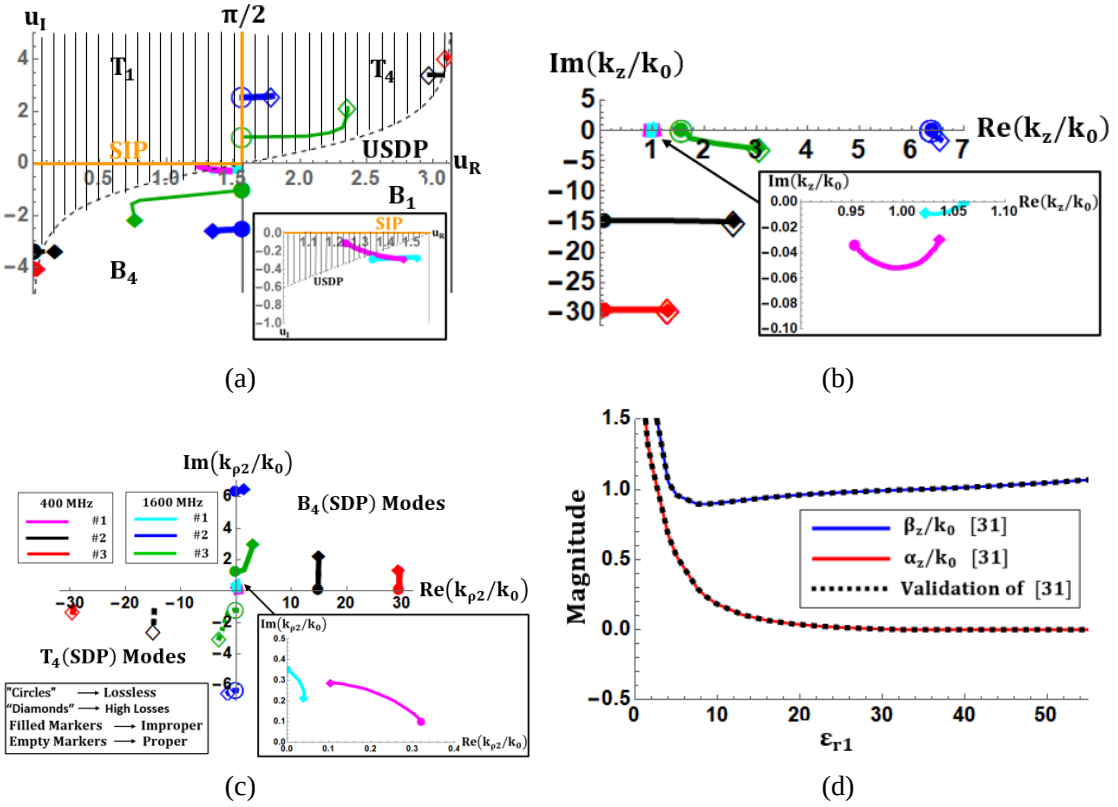

Figure 4. TM poles' trajectories following a complex relative permittivity increase of $\varepsilon''_{r1} = 0$ to 76 at $f = 400$ MHz on: (a) SDP plane, (inset: focus on #1 mode's trajectory), (b) k_z-plane (inset: focus on #1 mode's trajectory), (c) $k_{\rho 2}$ plane (inset: focus on #1 mode's trajectory), where with continuous and dashed curves are marked B_4 and T_4 modes respectively. Common index of Figs. 4(a)–(c) in the last figure, (d) verification of dominant pole's movement with results of [31].

The pole's (k_{zp}) contribution is taken into account regardless its position as depicted in Equation (12), where the ordinary residue $L(k_{zp})$ is modified to account for its proximity to the saddle point θ_c (observation angle). A maximum contribution occurs when $k_{zp} = k_0 \sin\theta_c = real$, equivalent to $u_{Rp} = \theta_c$, which becomes more intense as the imaginary part of k_{zp} is minimized (closing to the real axis). From this point of view, the contribution of the dominant pole at 1600 MHz is expected to be higher than that at 400 MHz, as its trajectory is closer to the real axis (Figs. 2–3). A strange situation occurs when the pole approaches the branch point at $k_z = k_0$ where maximum leakage is expected as θ_c tends to 90°. Then Equation (10) becomes indefinite as 0/0, but taking the limit $k_{zp} \to k_0$ and $\theta_c \to \pi/2$ using L'Hospital rule, and then Eq. (10) yields the expected maximum toward the endfire for

the dominant mode as:

$$F_p(\theta_c = \pi/2, k_{zp} = k_0) = \lim_{\substack{\theta_c \to \pi/2, \\ k_{zp} \to k_0}} F_p(k_0 \sin\theta_c) \overset{\text{L'Hospital}}{=} \lim_{\substack{\theta_c \to \pi/2, \\ k_{zp} \to k_0}} \left(\frac{\left(\varepsilon_{r1} + 2\cos^2\theta_c - 1\right) \cdot 2L_p}{2\cos\theta_c \sqrt{\varepsilon_{r1} - \sin^2\theta_c}} \right) \quad (16)$$

which tends to infinity at this limit.

Substituting the values $\theta_c = \theta_{c,\max}$ for the dominant mode #1 in Table 1, the limit reads:

(i) $f = 400\,\text{MHz}$: $\theta_c = \theta_{c,\,\max} = 84.25^\circ \rightarrow L_1 = L(k_{z1}) = 0.0012$ and $F_{p1,\max} = 0.087$.

(ii) $f = 1600\,\text{MHz}$: $\theta_c = \theta_{c,\,\max} = 87.77^\circ \rightarrow L_1 = L(k_{z1}) = 0.0041$ and $F_{p1,\max} = 0.303$.

At this point, it would be interesting to examine the dominant energy leakage using the theory developed by Frezza et al. [17–20], although this is established for a planar dielectric interface.

In order to verify the dominant pole's movement, its position in the λ-domain is tracked when the real part of dielectric constant varies from 1 to 58.1 in Fig. 4(d). In this way, the dominant mode's curve is verified with the respective one studied by Singh et al. [31]. The condition $a/\lambda_0 = 0.0667$, which is used therein [31], answers to operating frequency 727 MHz for the human arm model cylinder. However, the most significant verification of the validity of poles' positions constitutes the radiation results of Section 4, where it is indeed proved via Equation (9) that they compose the total far field given by expressions (3)–(4).

3.3. Dominant Leaky Mode Penetration-Leakage

The group of Frezza and his colleagues [17–20] considered an inhomogeneous plane wave incident at the planar interface of the lossy media as shown in Fig. 5(a). Enforcing the boundary condition (or the Snell law and the separability condition) at the interface, the Authors were able to identify a specific angle of incidence at which the wave could propagate (penetrate) inside the highly lossy medium without attenuation. Based on the reciprocity theorem, this phenomenon is expected to occur also herein. Namely, a wave emanating from a source inside the highly lossy medium and propagating at the predicted angle (specific phase constant $\beta_z = k_1 \cos\theta$) would exhibit zero (or small) attenuation constant and would be transmitted to the low-loss medium without any attenuation away from the interface. The question herein is whether the observed dominant leaky wave obeys the condition predicted by Frezza et al. [17–20]. To address this question, the lossy cylinder is assumed as medium #1 and the

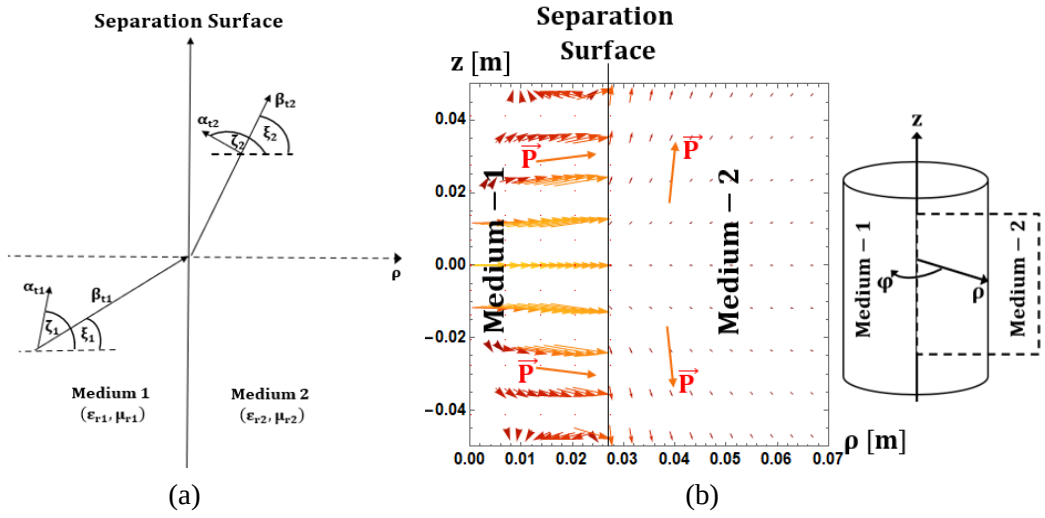

Figure 5. (a) Scattering of inhomogeneous wave on an interface between a highly lossy medium-1 and a low-loss medium-2, (b) Poynting vector representing the energy delivered from highly lossy medium-1 ($\rho < \alpha$ in Fig. 1) by the dominant improper mode (#1 in Table 1).

air as medium #2 (Fig. 5). The propagation constant along the direction of propagation (along a ray) is equal to the wavenumber $\vec{k}_{ti} = \vec{k}_i = \vec{k}_z + \vec{k}_\rho$ and $k_{ti} = \beta_{ti} - j\alpha_{ti}$, $i = 1, 2$, where for medium-1 $\vec{k}_{t1}$ is complex, while for medium-2, $k_{t2}^2 = k_0^2 =$ real. Notably, medium-2 is lossless thus $\beta_{t2} \perp \alpha_{t2}$ or $\zeta_2 - \xi_2 = \pi/2$, but medium-1 is lossy, thus β_{t1} and α_{t1} are not orthogonal. Transferring the analysis of [19] for the symbols utilized herein, it reads:

$$\beta_{t1}^2 - a_{t1}^2 = \mathrm{Re}\left(k_1^2\right) = \mathrm{Re}\left(k_0^2 \varepsilon_{r1}\right) \text{ and } 2\beta_{t1} a_{t1} \cos\left(\zeta_1 - \xi_1\right) = \mathrm{Im}\left(k_1^2\right) = \mathrm{Im}\left(k_0^2 \varepsilon_{r1}\right) \tag{17a}$$

$$\beta_{t2}^2 - a_{t2}^2 = \mathrm{Re}\left(k_2^2\right) = \mathrm{Re}\left(k_0^2 \varepsilon_{r2}\right) \text{ and } 2\beta_{t2} a_{t2} \cos\left(\zeta_2 - \xi_2\right) = \mathrm{Im}\left(k_2^2\right) = \mathrm{Im}\left(k_0^2 \varepsilon_{r2}\right) \tag{17b}$$

The optimum angle of incidence for the above phenomenon to occur is given in [18, Eq. (8)] or [20, Eq. (25)] as:

$$\tan \xi_1^{op} = \frac{\tan \eta_1 \pm \sqrt{\tan^2 \eta_1 - 4\chi\left(\chi - 1\right)}}{2\left(\chi - 1\right)} \tag{18}$$

where $\chi = \frac{\mathrm{Im}(k_2^2)}{\mathrm{Im}(k_1^2)}$ and $\eta_1 = \zeta_1 - \xi_1$. If ξ_1^{op} is sufficiently small, the small argument approximation [52] (from Taylor expansion) gives $\tan \xi_1^{op} \approx \xi_1^{op}$ [rad], and the latter can be used in Eq. (18). Substituting the values for the mediums-1, 2 of the dielectric waveguide of Fig. 1 and the dominant mode propagation constant from Table 1 in Eq. (18) yields for the two frequencies:

(i) $f = 400\,\mathrm{MHz}$, $\varepsilon_{r1} = 58.1 - j76$, $k_{t1}/k_0 = 8.78 - j4.36$, $k_{\rho 1}/k_0 = 8.717 - j4.36$, $\chi = 0$ since $\mathrm{Im}(k_2^2) = 0$, $\zeta_1 \to 0^\circ$, $\xi_1^{op} = 6.8^\circ$, $\eta_1 = \zeta_1 - \xi_1^{op} \approx -6.8^\circ$, $\xi_2^{op} = 84.25^\circ$, $\zeta_2^{op} = 90^\circ + \xi_2^{op} = 174.25^\circ$.

(ii) $f = 1600\,\mathrm{MHz}$, $\varepsilon_{r1} = 58.1 - j19$, $k_{t1}/k_0 = 7.72 - j1.23$, $k_{\rho 1}/k_0 = 7.65 - j1.23$, $\chi = 0$ since $\mathrm{Im}(k_2^2) = 0$, $\zeta_1 \to 0^\circ$, $\xi_1^{op} = 7.5^\circ$, $\eta_1 = \zeta_1 - \xi_1^{op} \approx -7.5^\circ$, $\xi_2^{op} = 87.7^\circ$, $\zeta_2^{op} = 90^\circ + \xi_2^{op} = 177.7^\circ$.

The above values exactly confirm the angle of maximum radiation-leakage of the dominant mode as predicted in Table 1, $\theta_{c,\max} = \xi_2^{op} = 84.2^\circ$ at 0.4 GHz and $\theta_{c,\max} = \xi_2^{op} = 87.7^\circ$ at 1.6 GHz. At $f = 0.4\,\mathrm{GHz}$, the Poynting vector of #1 mode in mediums-1 and -2 is evaluated and plotted using Eq. (10) and (Eq. (C3) in Appendix C). It is clearly observed in Fig. 5(b) that the Poynting vector, which is indexed as vector $\vec{P}$ in Fig. 5(b), is almost normal to the interface in the lossy region-1, while it tends toward the axial direction (parallel to the interface) in the lossless region-2. The Poynting vector at mediums 1 and 2 form the same angles $\xi_1 = 6.8^\circ$ and $\xi_2 = 84.25^\circ$ as indicated in Fig. 5(b). These coincide identically with the wave fronts' angles $\xi_{1,2}^{op}$ from Frezza's expression (18), as also defined by the phase vectors of the waves propagating in the two media (Fig. 5(a)). Besides that, its amplitude (length of arrows) is retained almost constant (unattenuated) in the lossy region-1 ($\rho < \alpha$).

3.4. Increasing Losses Break the Symmetry of Quadruplets Complex Modes

As explained before, the axially symmetric excitation of Fig. 1 supports only TM_{0n} modes, among which there are no complex quadruplets. However, it is interesting to study the effects of high losses on them. For this purpose, the hybrid EH_{12}^z case is tracked in Fig. 6(a) as ε_{r1}'' is increased from zero to 76 for 400 MHz, and the hybrid EH_{17}^z case is tracked in Fig. 6(b) as ε_{r1}'' is increased from zero to 19 for 1600 MHz. Specifically, the hybrid modes EH_{12}^z and EH_{17}^z were found to behave as complex quadruplets. As expected for the lossless case, ($\varepsilon_{r1} = 58.1 - j0$), a perfect symmetric quadruplet EH_{12}^z or EH_{17}^z complex mode set ($\pm k_z, \pm k_z^*$) is observed at points A, B, C, D of the inset in Fig. 6. It is well understood that the net energy (or the total Poynting vector) carried by this symmetric set is zero, e.g., [13]. However, as losses are increased the symmetry breaks down leading to points (A′, B′, C′, D′) in Fig. 6, which is in accordance to Kamel and Omar [16] who already studied a similar phenomenon, but for a planar structure. It is observed that the pair of modes B, D move on the imaginary axis of k_z becoming purely attenuated waves. On the contrary, the pair A, C retain almost the same imaginary part of k_z and move to highly increased real k_z. Hence, the pair (A′, C′) is then an ordinary forward and reverse propagating set of modes, which may carry a net energy or radiate when the poles are located close to the saddle point as explained in the previous paragraphs.

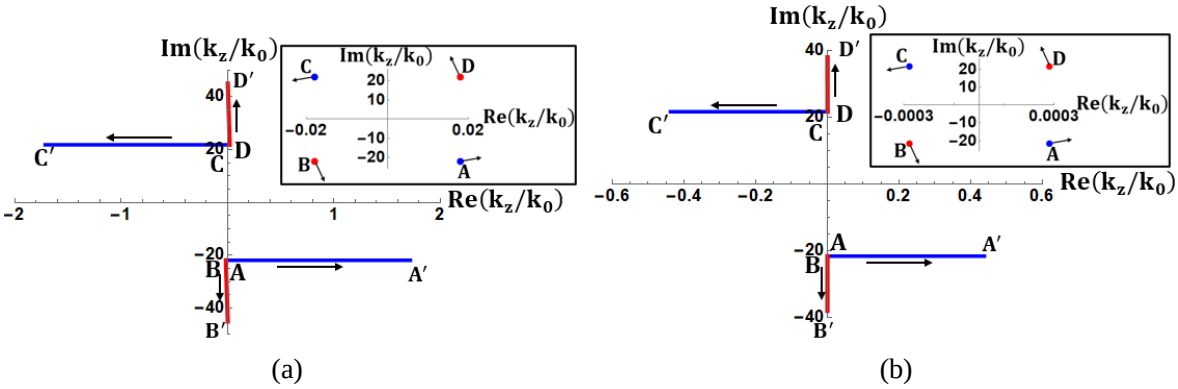

Figure 6. Behavior of a quadruplet of complex poles on k_z-plane: (a) 400 MHz, (b) 1600 MHz as dielectric losses increase. A, B, C, D positions of poles respond to the lossless case, while A′, B′, C′, D′ respond to the lossy cases of 400 and 1600 MHz arm-model. In the insets the initial symmetrical positions are presented.

4. NUMERICAL RESULTS-VALIDATION

The proposed methodology addressing the mode transition due to the extremely high losses of high dielectric constant biological cylinders will be validated in this section. For this purpose, both the discrete and continuous spectra are evaluated keeping a mind that the ultimate aim is to identify the optimal technique for maximizing the electromagnetic energy-signal transferring inwards or outwards from biological cylinders. In order to validate the proposed method as well as to establish a reference, a lossless cylinder studied in [31] is first elaborated. In turn, a cylindrical human arm model is examined mainly at the characteristic frequencies of 400 and 1600 MHz.

4.1. Validation against a Lossless Cylinder

The lossless cylinder studied in [31] has a radius $a = 0.0667\lambda_0$ (λ_0 the free space wavelength) and a varying real dielectric constant taking values as $\varepsilon_{r1} = 9.8$, 13, 22, 33. Again, excitation by a z-oriented infinitesimal dipole is assumed, which is placed at the axes' origin. The three first possibly excited TM^z modes are presented in Table 2, but only for the highest dielectric constant $\varepsilon_{r1} = 33$. Notably, all modes existing in this case are of improper nature, and they occur below the cut-off frequency of the first proper guided mode. It is again justified that the dominant mode is of leaky wave type, and it has an axial propagation constant slightly smaller than the free space wavenumber ($\beta_{zp} = k_0^-$). Since $k_{zp}^2 = k_0^2 - k_{\rho 2}^2$, the corresponding $k_{\rho 2}$ tends to zero, thus the leaky electromagnetic energy will be directed parallel to the cylinder's surface. As described in the previous Section 3 and proved by Frezza et al. [18–20], this leaky mode provides the capability for "deep penetration" into lossy media. However, the work of Singh et al. [31] reveals that the same phenomena occur for any dielectric constant for both lossy and lossless media. Thus, its propagation constant is estimated and depicted in Table 3.

Table 2. First three leaky waves' normalized propagation constant for dielectric constant $\varepsilon_{r1} = 33$ and cylinder's radius $\alpha = 0.0667\lambda_0$. The switching criterion for transition function argument is $z_p \leq 2$.

Mode Number	k_z/k_0	$k_{\rho 2}/k_0$	u_R	u_I	Maximum at angle θ_c	Transition Function Argument
#1	$\pm 0.9985 \mp j0.00068$	$0.056 + j0.0121$	$\pm 86.8°$	$\mp 0.69°$	$\pm 86.8°$	1.22
#2	$\pm 0.119 \mp j7.133$	$7.203 + j0.1178$	$\pm 0.947°$	$\mp 152.57°$	$\pm 0.947°$	68.8
#3	$\pm 0.082 \mp j15.73$	$15.762 + j0.082$	$\pm 0.298°$	$\mp 197.65°$	$\pm 0.298°$	145.9

Table 3. Dominant leaky wave's normalized propagation constant with respect to the cylinder dielectric constant, ($\alpha = 0.0667\lambda_0$). The switching criterion for transition function argument is $z_p \leq 2$.

ε_{r1}	k_z/k_0	$k_{\rho 2}/k_0$	u_R	u_I	Maximum at angle θ_c	Transition Function Argument
9.8	$\pm 0.9015 \mp j0.186$	$0.5586 + j0.3002$	$\pm 58.22^\circ$	$\mp 19.84^\circ$	$\pm 58.22^\circ$	4.88
13	$\pm 0.9234 \mp j0.1065$	$0.4535 + j0.2168$	$\pm 63.84^\circ$	$\mp 13.71^\circ$	$\pm 63.84^\circ$	3.86
22	$\pm 0.9696 \mp j0.0267$	$0.2648 + j0.0977$	$\pm 74.72^\circ$	$\mp 5.79^\circ$	$\pm 74.72^\circ$	2.4
33	$\pm 0.9985 \mp j0.00068$	$0.0561 + j0.0121$	$\pm 86.8^\circ$	$\mp 0.69^\circ$	$\pm 86.8^\circ$	1.22

Additionally, its contribution to the leaked far field can be estimated through the pole contribution as $F_p/\cos\theta_c$ which is identical to the one evaluated in [31] (since the $\cos\theta_c$ term inside Eq. (10) is not encountered in [31] also). It is important to note that this pole contribution is composed of the ordinary residue, but as modified in Equation (10), so as to account for its proximity to the saddle point similar to Ostner et al. [25] or Collin and Zucker [10, Part II, Ch. 20.2]. The corresponding maximum occurring at θ_c defined in Eq. (12) is also shown in Table 3. As proved by Frezza et al. [18–20], this mode may be excited by a wave incident at the critical angle thus in Eq. (18) above it is ξ_{opt}, which is also utilized in [31]. The resulting contribution in the far field is illustrated in Fig. 7(a), where it is observed that besides the beam toward θ_c caused by the forward propagation, a similar beam toward $-\theta_c$ appears due to the symmetrical propagation of $k'_{zp} = -k_{zp}$ toward negative z. In turn, the total

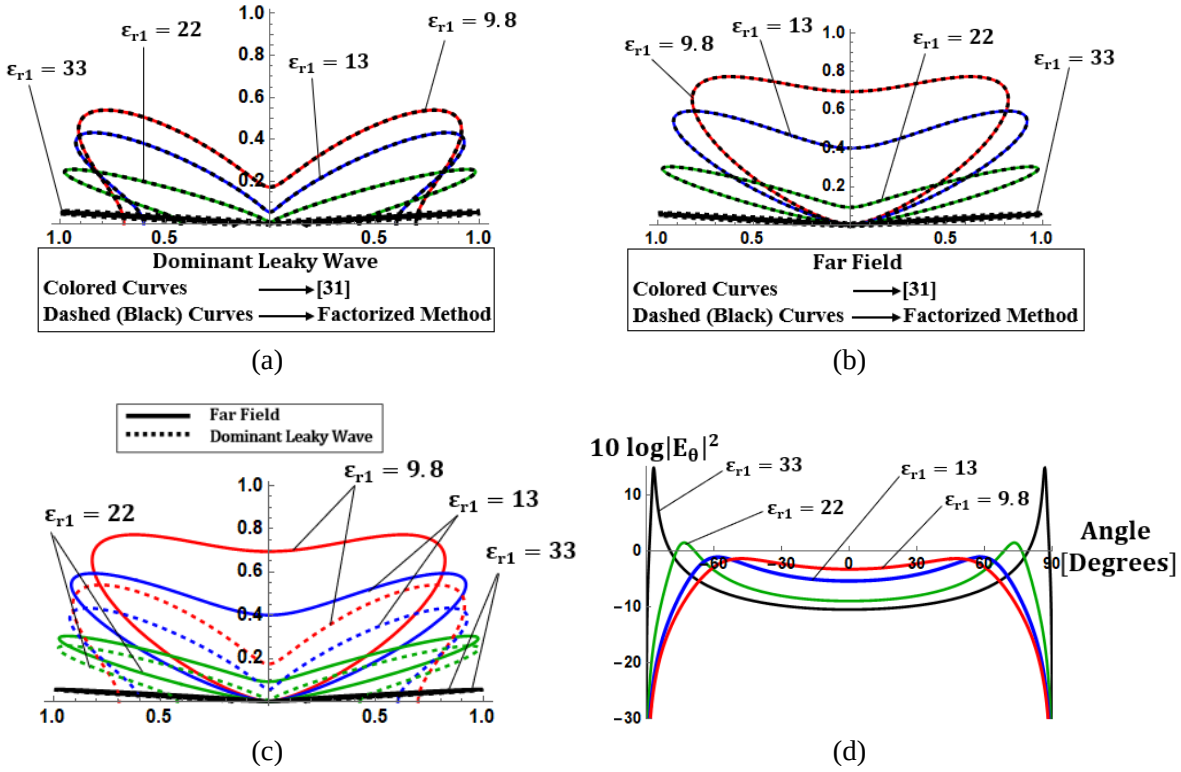

Figure 7. Comparison of present results (dashed black curves) with the ones (colored curves) of [31] for different cylinder's dielectric constant and radius $a = 0.0667\lambda_0$: (a) Normalized, (to its maximum value), dominant leaky wave power radiation pattern, (b) total far-field power radiation pattern normalized to its maximum value, (c) comparison of dominant leaky wave versus total far field power patterns, (d) logarithmic representation of far field power pattern.

radiated far field is calculated according to the proposed formulas of Eqs. (8)–(9). The results are compared in Fig. 7(b) against those of [31] and observed to be identical, while dominant leaky wave and total far field patterns are compared against each other in Fig. 7(c). A significant dominant mode's contribution from Equation (9) toward the broadside direction is observed in Fig. 7(b), along with a minor contribution of the high order modes of Table 2. The total far field is illustrated in logarithmic scale [dB] in Fig. 7(d) which reveals that as the dielectric constant is increased, the first leaky wave dominates; the beam directivity is increased; the maximum turns towards endfire.

Evaluating the trajectory of the dominant leaky mode in Fig. 8(a) by varying the real part of dielectric constant ε_{r1} as in [31] reveals that this mode belongs to the fast-wave improper region and is always captured in this range by upper SDP path. Although the dominant mode is captured by the USDP path, it is relatively close to the saddle point ($\lambda = k_z/k_0 = 1$). Hence, its proximity to the saddle point is expected to affect the resulting radiated field. This could make the classical SDP inaccurate, and (according to our previous arguments) either the generalized formulas (13)–(14) or the proposed herein Eq. (9) should be employed. However, the classical SDP was utilized in [31], and their results are validated by the commercial stimulator HFSS. Phenomenically, this contradicts the claim that classical SDP fails when poles are in proximity to the saddle point. However, Senior and Volakis [Fig. 3.12 in p. 66, 50] therein depict that the transition function tends to unity $F_{KP}(z_p^2) \to 1$ as its argument z_p is increased and reaches 0.99 for $z_p = 2$. A similar proof is given by Daniele and Zich [53, p. 44]. Besides that, the F_{KP} argument involves a limiting approach as $r \to \infty$, (far field), and a pole proximity to observation angle θ_c, which correspondingly yields $b_p \to 0$ as defined in Equation (13). Thinking on how to reveal the proximity effect and since the pole location depends on a lot of structures' parameters, we decided to examine it for a near (at $k_0 r = 2$, performing a numerical integration via Romberg

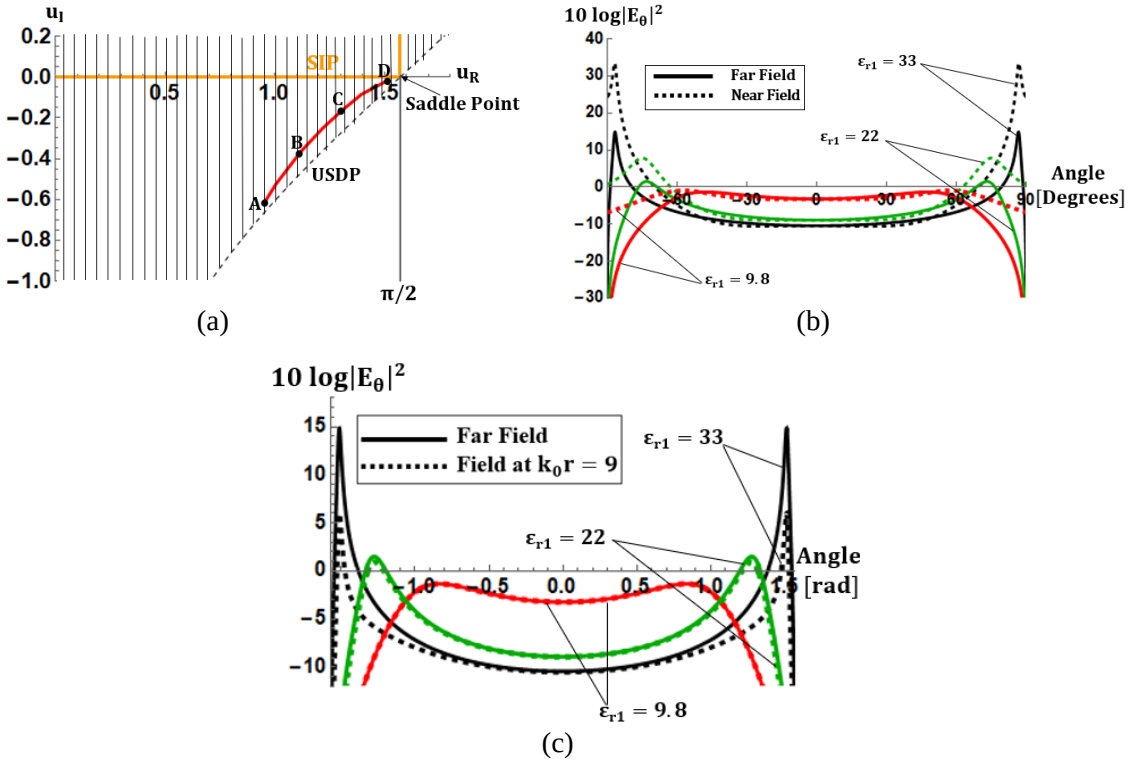

Figure 8. (a) Trajectory (red curve) of the dominant leaky wave of Table 3, varying real permittivity. Shadowed region denotes the region where poles may be captured among the SIP and USDP paths, while points A, B, C and D denote the positions for the examined dielectric constants $\varepsilon_{r1} = 9.8$, 13, 22, 33 respectively. (b) Near field at $k_0 r = 2$ versus the total far field (continuous curve) for different cylinder's dielectric constants. (c) Intermediate field (dashed curves) at $k_0 r = 9$ compared against the total far field (continuous curve) for cylinder's dielectric constants $\varepsilon_{r1} = 33$.

method) and intermediate field (at $k_0 r = 9$, employing saddle point method). The latter corresponds to a transition function loss of -8 dB only for the case $\varepsilon_{r1} = 33$, and transition functions F_{KP} argument $z_p = 4.88$, 3.86, 2.4, and 1.22 (values over the angular range) for $\varepsilon_{r1} = 9.8$, 13, 22, and 33, respectively. The resulting total field from Equation (14), given by [50] and the herein proposed Eq. (9) are depicted in Figs. 8(b)–(c) and compared against the far field of Fig. 7(d). It is clearly evident from Fig. 8(c) that significant changes are observed around the angle of dominant mode maximum. Notably the difference between the intermediate (e.g., $k_0 r = 9$) and far field, ($k_0 r \to \infty$), are more pronounced for the case $\varepsilon_{r1} = 33$ where the argument of F_{KP} is $z_p = 1.22$, thus less than 2. On the contrary for the other cases of $\varepsilon_{r1} = 9.8$ and 22, negligible differences are observed as $z_p > 2$. Although this is an indirect comparison, it is appropriate for the scope of this work which primarily aims at the near and intermediate field around cylinders modeling human organs. The near field of the cylindrical model elaborated in [31] for cylinder's radius $a = 0.0667\lambda_0$ is evaluated in Fig. 8(b) and compared to the far field in logarithmic scale. It is clear that significant deviation between the intermediate ($k_0 r = 9$) and far field is observed only around the radiated beam maximum and thus is due to the proximity of the pole u_p to the saddle point.

4.2. Near and Far Field Around the Human Arm Model

4.2.1. Far Field

a) Effect of Losses on Modal Contributions

The TM^z modes possibly excited by the z-oriented infinitesimal dipole placed at the origin are already depicted in Table 1, as explicitly analyzed in Section 3. The dominant mode trajectory, when losses are increased, crosses the USDP when $\varepsilon''_{r1} = 27$, or $\tan\delta = \varepsilon''_{r1}/\varepsilon''_{r1} = 0.4647$. Thus, beyond that and for the human arm (biological) losses $\varepsilon''_{r1} = 76$ this pole is located beyond SDP, and it is thus not captured. However, it may still contribute to the radiated field depending on its proximity to the USDP and particularly its location with respect to the saddle point, e.g., [10, Part II, Ch. 20.2]. Its contribution can be calculated by Eq. (9) proposed herein, as well as by Eq. (14) [50].

Explicitly, for the human arm model, the dominant mode's axial propagation constant becomes slightly higher than the free space wavenumber, as $k_z/k_0 = 1.0363 - j0.0292$ (400 MHz, $\varepsilon_{r1} = 58.1 - j76$) or $1.0223 - j0.0084$ (1600 MHz, $\varepsilon''_{r1} = 58.1 - j19$). Thus, it becomes a slow wave ($u_p < c$), which is not captured from SDP path, but it retains a small imaginary part. Hence, it is expected to retain its almost (axial) endfire radiation beam at angles close to 90°. Its contribution F_p, evaluated from Eq. (10) for the dominant mode, at 0.4 and 1.6 GHz is depicted in Figs. 9(a)–(b), where the corresponding maxima are observed at $\theta_{c,\,\text{lossy}} = 84.25°$ (0.4 GHz) or 87.77° (1.6 GHz). At both operating frequencies, the lossless case $\varepsilon''_{r1} = 0$, (where the pole is captured by SDP), is depicted for the comparison in Figs. 9(a)–(d) for which the corresponding total field maxima are oriented toward $\theta_{c,\,\text{lossless}} = 71.38°$ (400 MHz) or 70° (1600 MHz). The total far field calculated from Eqs. (8) and (9) is also depicted in Fig. 9 by continuous curves. It is important to note that the increase in losses, while it retains almost the same maxima directions, but it significantly altered the radiation-leakage toward other directions, including the broadside where the radiated field is not zero anymore, but it has a significant value by 84% (400 MHz) and 71.4% (1600 MHz) below the maximum. While the absolute field values shown in Figs. 9(a)–(b) depict the effect of losses, it would be interesting to examine the normalized radiation pattern given in Figs. 9(d)–(e), in polar coordinates. At 400 MHz, the normalized radiation increases toward broadside when losses are increased, but the opposite happens at 1600 MHz. This is a direct consequence of the opposite behavior of the dominant mode behavior (Figs. 9(a)–(b)) resulting from its pole location (Fig. 4). Besides the dominant improper (leaky) mode, higher order modes of the same character are classified in Table 1 according to an increasing attenuation constant. These are also expected to contribute to energy leakage both in the near or far field and are already included in the total field of Fig. 9; however, they should be examined separately. Their contribution calculated using Equation (10) and their overall sum manipulated as in Eq. (9), provide the second term of Eq. (11), which is plotted in Figs. 10(a)–(b), at both 0.4 and 1.6 GHz. It is important to observe that although their maximum occurs at broadside, their overall contribution is much lower than that of the dominant leaky mode, even at broadside.

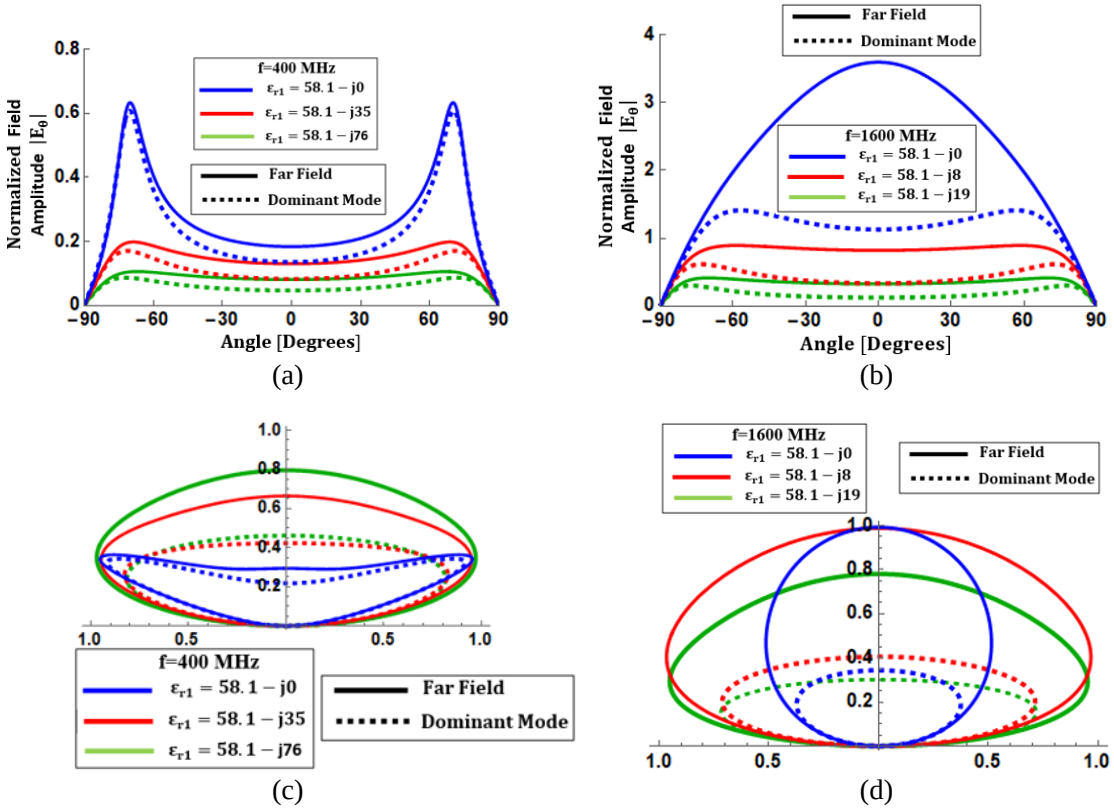

Figure 9. Total far field (continuous curves) pattern of $|E_\theta|$ and dominant leaky pole's (dashed curves) radiated field versus variations of internal medium's losses (ε''_{r1}) at: (a) 400 MHz, (normalized to $g(\alpha)\frac{e^{-jk_0 r}}{r}$), (b) 1600 MHz, (normalized to $g(\alpha)\frac{e^{-jk_0 r}}{r}$), (c) 400 MHz, (normalized to maximum values), (d) 1600 MHz, (normalized to maximum values). The angle is measured with respect to the normal to cylinder's surface.

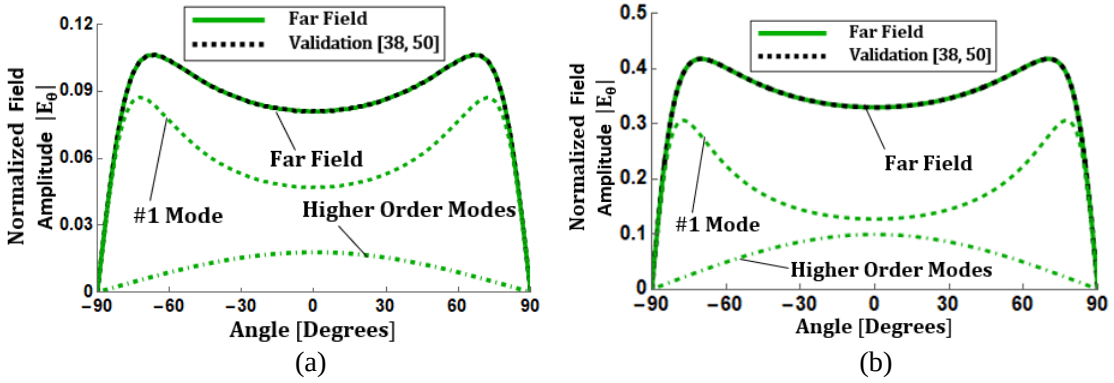

Figure 10. Far field radiation pattern of $|E_\theta|$ for the human arm cylinder, (normalized to $g(\alpha)\frac{e^{-jk_0 r}}{r}$), versus the observation angle, which is defined with respect to the normal, (to cylinder's interface), axis, (a) at 400 MHz, (b) at 1600 MHz.

b) Effect of Losses on Continuous Spectrum

The next task refers to the examination of how the losses affect the branch-cut integral namely the space wave radiation or the continuous spectrum. For the proposed method, branch-cut contribution could be identified by "F_{branches}" in Eqs. (8) to (9). Its normalized value is given by $\exp[q_+(\lambda)+q_-(\lambda)]$ in

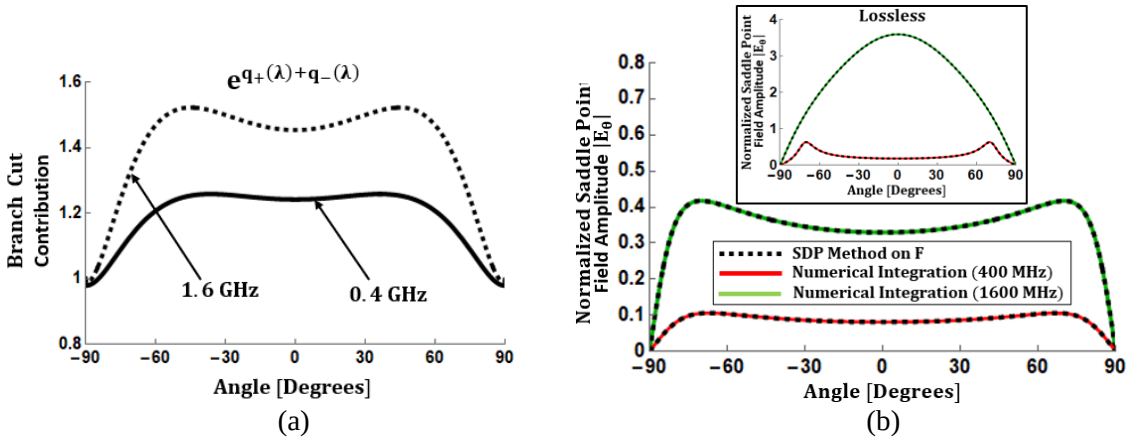

Figure 11. (a) Contribution of term $\exp[q_+(\lambda) + q_-(\lambda)]$ at 400 and 1600 MHz operating frequencies. (b) Contribution from both F_{poles} and F_{branches} into space wave and validation of the current factorized method versus the SDP space-wave at 400 and 1600 MHz, inset: lossless cylinder's space wave validation.

Eq. (9) and is evaluated for the two operating frequencies in Fig. 11(a). Correspondingly in the classical SDP, the space wave is defined by the second term of Eq. (11). For the established general case, we employ the "additive" approach in Eq. (14) which is already proved to be equivalent to the general multiplicative method in Eq. (13). In this approach, the space wave includes the effect of the poles as the branch cut integral which is clearly indicated by the presence of the sum terms within the brackets of Eq. (14a). This is the only difference from the classical SDP approach of Eq. (11). Comparing the multiplicative method proposed herein Eq. (9) with the classical one Eq. (11), it is not possible to make a one-to-one correspondence and thus is also impossible compared to the "additive" method in Eq. (14). However, examining Eq. (9) it is clear that $F_{\text{branches}} = \exp[q_+(\lambda) + q_-(\lambda)]$ represents the branch cut integral in the absence of zeros and absence of poles. In the established methods of literature [38, 39], performing a saddle point integration of the field defined by function F along the SDP contour $\cos(u_R - \theta_c) \cdot \cosh(u_I) = 1$ provides the space wave. Herein, the SDP method is performed along the same path in function F, but on its factorized expression of Eqs. (8)–(9), as $F = F_{\text{poles, zeros}} \cdot F_{\text{branches}}$, as the second term of expression (11) indicates. Thus, leaky waves fall into the second term of (14) [29, 30], being evaluated together with F_{branches} into the space wave term. The latter multiplicative form expression proves that poles also contribute to the continuous wave by virtue of their proximity to the branch cut integral, similar to the additive expression of [51]. We expect that the complete expression (9) will give the same results as the general approaches of Eq. (13) or (14). For a more concrete proof, these must be compared numerically on the factorized expression of F. For this purpose, the space wave term is compared against SDP integral in Fig. 11(b) for the 0.4 and 1.6 GHz frequencies. It is observed that indeed the two results are almost identical. In turn the total far field expressions including the modal contribution F_p of Eq. (10) and branch-cut contribution are calculated using the three formulas (9), (13), and (14) for both the lossless and lossy cases and at the two operating frequencies of 0.4 and 1.6 GHz. The results are depicted in Figs. 11(a)–(b). The transition functions in Eq. (13c) do not introduce any changes into the space wave term, thus the result obtained from Eq. (11) coincides to the space wave term obtained from Eqs. (13) and (14).

Searching for a case, when the transition functions correct the field for the human arm geometry structure, a lossless dielectric constant of $\varepsilon_{r1} = 36.5$ is chosen at 1600 MHz, where the argument of F_{KP}, $z_p = 0.9$, is less than 2. It is clear from Fig. 12(a) that significant deviation between the intermediate field at $k_0 r = 8$ and far field is observed only around the radiated beam maximum and thus is due to the proximity of the pole u_p to the saddle point. The resulting total far field from the method utilized in [50] and also presented herein in Equations (13)–(14) and the present method of Eq. (9) are compared against the result of the classical SDP method of Eq. (14) and also given in [38], for the case of $\varepsilon_{r1} = 36.5$ and $f = 1600$ MHz. The results are depicted in Fig. 12(b), where it is observed that indeed the classical SDP has a significant deviation (overestimation) in the field around the beam maximum (pole close to

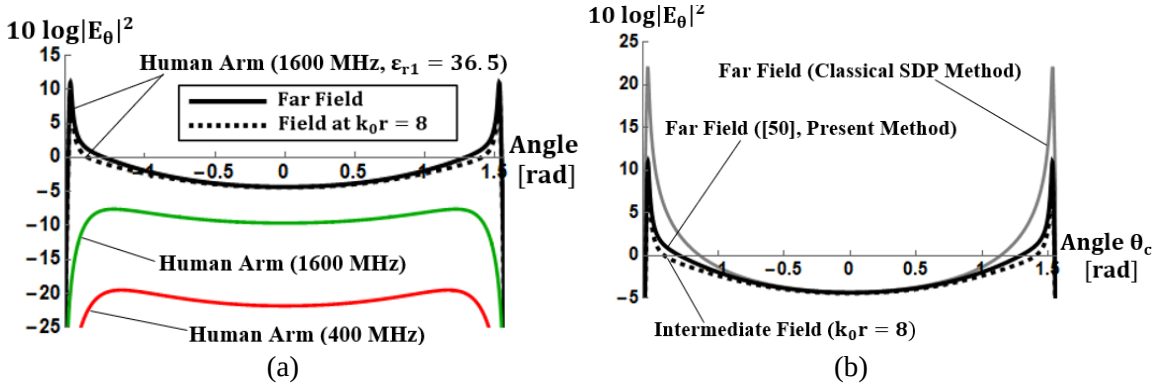

Figure 12. (a) Intermediate field (dashed curves) at $k_0 r = 8$ compared against the total far field (continuous curve) for a human arm cylinder geometry operating at 1600 MHz, filled with a lossless dielectric of $\varepsilon_{r1} = 36.5$. (b) Comparison of the far field obtained via different methods of literature [38, 50] and present method.

the saddle point), with respect to the generalized SDP [50] and proposed method in Eq. (9). On the contrary, the two latter methods are in excellent agreement and very close to the numerically calculated intermediate field ($k_0 r = 8$). Further investigation through numerical integration reveals that the results become identical to the far field asymptotic approximation, which is in accordance to [50].

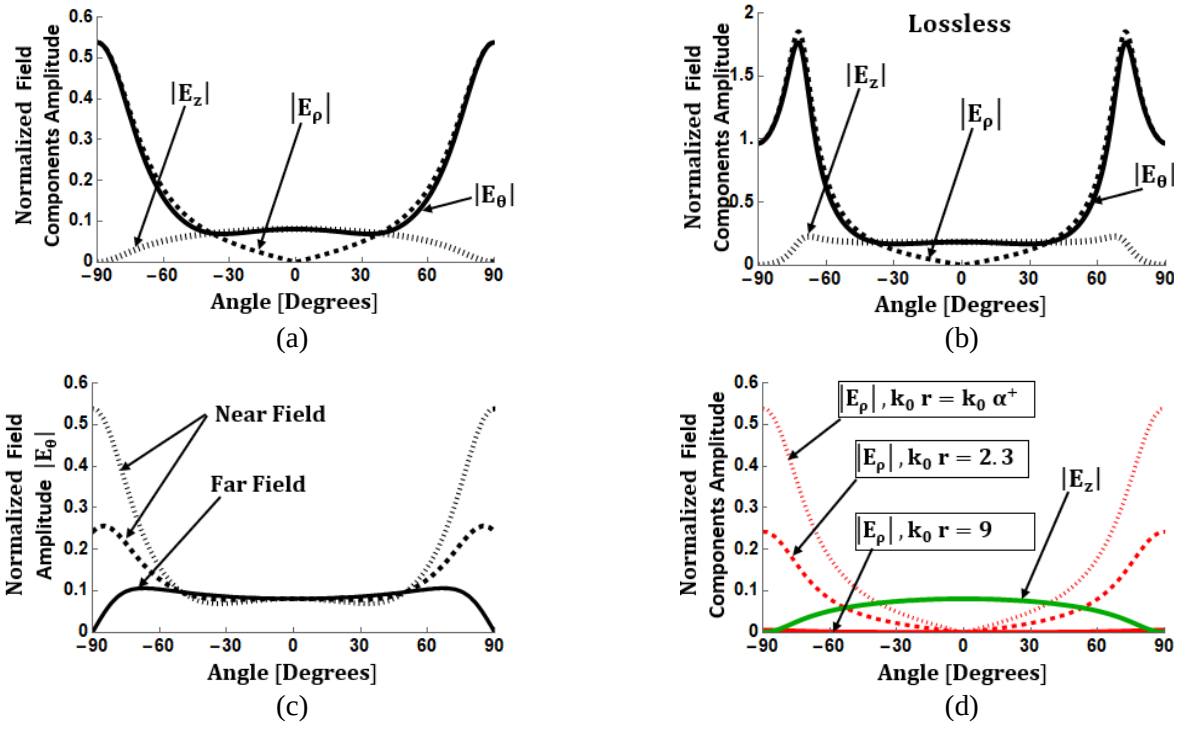

Figure 13. Electric field components at 400 MHz: (a) E_z, E_ρ and, (spherical), E_θ in the near field in the human arm model, ($\varepsilon''_{r1} = 76$), (b) E_z, E_ρ and, (spherical), E_θ in the near field in the lossless human arm model, ($\varepsilon''_{r1} = 0$), (c) variation of $|E_\theta|$: near cylinder's interface with tiny-dashed curve, at a distance not as far from cylinder's interface ($k_0 r = 2.3$) with heavy dashed curve and at larger distance ($k_0 r = 9$) with solid curve, (d) $|E_\rho|$, $|E_z|$ field pattern at near ($k_0 r = k_0 \alpha^+$, 2.3) and far field ($k_0 r = 9$).

4.2.2. Near Field

Since the present work elaborates on dielectric rod emulating biological organs, the near field is even more important than the far field. The implanted devices may aim at communications or energy transfer with wearable devices, (at a small distance forms the sum), or devices inside the room or on its ceiling. Then it is important to evaluate the near field as well as to estimate the distance at which this becomes the same as that approximated by the above far field approaches. For this purpose, the field expression for the E_θ component given in Eq. (9) can be utilized. However, the involved branch cut integrals must now be evaluated numerically along the original SIP path defined in Fig. 2. Although this integral is defined for the E_θ component in Eq. (9), it is relatively easy to isolate the corresponding Green's functions $G_2^{(0)}(k_z, \rho, \rho')$ for the air region-2, as explicitly shown in Appendix C. In turn, this is substituted in the general expression (1) to obtain the E_z and H_z components. Any field component can be estimated through the general relations between axial and transverse field components for cylindrical structures waveguides, e.g., Pozar [54] or from [35], for the lossy cylinders at 400 and 1600 MHz, as well as the lossless ones, ($\varepsilon''_{r1} = 0$). The required numerical calculations are carried out through Mathematica 11 [55], wherein a Romberg scheme is employed for the branch cut integral. All electric field components, (normalized to the term $g(\alpha)\frac{e^{-jk_0 r}}{r}$), are in turn calculated and illustrated in Figs. 13–14, at 0.4 and 1.6 GHz for distances $k_0 r = k_0 \alpha^+$, 2.3 and 9 where $\alpha = 2.75$ cm is the cylinder radius. The amplitudes of the three field components versus the angle θ_c are depicted in Figs. 13–14. First similar behavior is observed at the two frequencies, but the field is about five times stronger at 1.6 GHz with respect to that at 0.4 GHz. The axial field E_z is maximized at broadside ($\theta_c = 0°$), while the radial E_ρ and spherical E_θ components exhibit strong maximums toward the endfire $\theta_c = -90°$ and $+90°$. As expected, the radial field component decreases with an increase in the distance from the cylinder surface as shown in

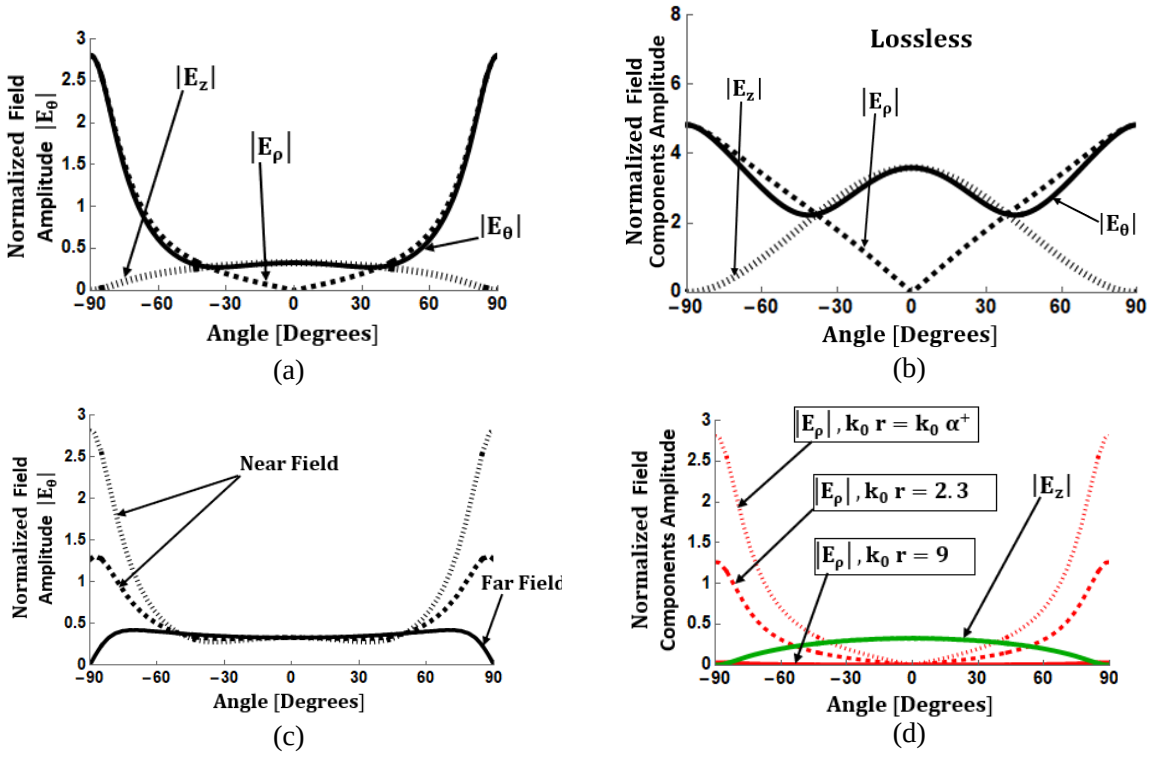

Figure 14. Electric field components at 1600 MHz: (a) E_z, E_ρ and, (spherical), E_θ in the near field in the human arm model ($\varepsilon''_{r1} = 19$), (b) E_z, E_ρ and, (spherical), E_θ in the near field in the lossless human arm model ($\varepsilon''_{r1} = 0$), (c) variation of $|E_\theta|$: near cylinder's interface with tiny-dashed curve, at a distance not as far from cylinder's interface ($k_0 r = 2.3$) with heavy dashed curve and at larger distance ($k_0 r = 9$) with solid curve, (d) $|E_\rho|, |E_z|$ field pattern at near ($k_0 r = k_0 \alpha^+$, 2.3) and far field ($k_0 r = 9$).

Figs. 13(d) and 14(d). Regarding the spherical E_θ component in Figs. 13(c) and 14(c), its amplitude at the endfire direction is gradually reduced to zero with an increasing distance. However, its values are retained almost constant toward broadside, while it becomes finally identical with the far field. The latter phenomenon is also verified by Sammut [56], who proves that up to a certain distance the leaky waves attenuate, while beyond that, they attain their far field characteristics.

Summarizing the above results, for near or far field, its intensity at 1600 MHz is approximately 4–5 times greater than that at 400 MHz. This is in accordance with Poon et al. [1–3], who on the basis of human phantom models (Debye or Cole-Cole [1–3]), proved that indeed the frequency range of 1.6–1.7 GHz becomes optimal, and explicitly in this range high leakage is expected. This peculiar phenomenon is due to the lower dielectric losses around 1600 MHz than those at lower frequencies like 400 MHz, as predicted by the Drude model [6]. While one expects losses to increase proportional to frequency a step back is observed in the range 1.6 to 1.7 GHz. However, as it is proved herein, at lower frequencies (like 400 MHz), the radiation mechanisms of the excited modes permit significant leakage (although smaller) provided that the dominant mode identified herein is efficiently excited. Thus, transferring energy inwards or outwards from the human body is possible at lower frequencies, but effectively only in the 1.6–1.7 GHz range.

5. CONCLUSION AND DISCUSSION

In this paper, the radiation characteristics of the discrete and continuous spectra for the "human arm infinite cylinder-rod model", excited by an infinitesimal dipole oriented along the symmetry axis-z and placed at axes' origin, are investigated. The above analysis has revealed the correlation of leaky modes' pattern with their positions in the complex steepest descent plane. The effects of dielectric losses in the radiation mechanisms are investigated through the poles' trajectory in the complex domain. However, an important feature of the current work arises from the numerical and analytical proof that indeed improper modes affect the formation of the space wave through a proposed field product representation. This field product stems from the Wiener-Hopf factorization of non-meromorphic functions and is capable of handling poles when they are either close to the saddle point (observation angle) or even outside the classical steepest descent capture zone. Although the proposed method is found herein to be equivalent to the "multiplicative" and "additive" steepest descent methods as summarized by Senior and Volakis [50], its derivation is more straightforward, and more importantly it can be utilized for both the far and near field evaluations. This is of particular importance in biomedical applications especially when implanted antennas are involved, where the near field is of primary significance. Furthermore, a very important low order leaky wave is encountered having very small attenuation constant and being capable of significant energy transferring inwards-outwards highly lossy dielectric cylinders. This is in accordance with the findings of Frezza et al. [17–20] who proved the existence of a deeply penetrating inhomogeneous wave into planar highly lossy structures when it impinges at a specific angle. Finally, the observation of Poon et al. [1–3] that the optimum frequency range for energy-signal transferring inwards-outwards biological tissues occurs around 1.6 GHz is also verified, but it is herein pointed that this is again due to the previously mentioned dominant leaky mode.

Overall, it is herein proved that indeed it is possible to transfer energy inwards-outwards highly lossy biological cylinders at specific frequencies and by a specific leaky wave. Also, the proposed field product representation is equivalent to generalized steepest descent methods in handling the far field, but it additionally offers a convenient near field evaluation.

APPENDIX A. FIELD PRODUCT REPRESENTATION

The factorization presented in this appendix is identical to the one utilized in Wiener-Hopf problems following [40] and [42]. It is well known that every meromorphic function can be written in the form [57, p. 116]:

$$\frac{1}{2\pi j}\int\limits_{C}\frac{K'(x)}{K(x)}\,\varphi(x)dz=\sum_{n=1}^{N}\varphi(k_{zn})-\sum_{p=1}^{P}\varphi(k_{zp}) \tag{A1}$$

where k_{zn}, (k_{zp}), denote the n-th, (p-th), root, (pole), of the K function. Note that if we chose in Eq. (A1) as φ the function $\left[\ln\left(1+\frac{\lambda}{x}\right)-\frac{\lambda}{x}\right]\frac{K'(x)}{K(x)}$, the following holds:

$$\exp\left(\frac{1}{2\pi j}\int\limits_{C}\left[\ln\left(1+\frac{\lambda}{x}\right)-\frac{\lambda}{x}\right]\frac{K'(x)}{K(x)}\,dx\right)=\frac{\prod\limits_{n=1}^{+\infty}\left(1+\frac{\lambda}{k_{zn}}\right)e^{-\frac{\lambda}{k_{zn}}}}{\prod\limits_{p=1}^{+\infty}\left(1+\frac{\lambda}{k_{zp}}\right)e^{-\frac{\lambda}{k_{zp}}}} \tag{A2}$$

where C is a path enclosing all singularities of K. On the other hand, an entire function takes the form [42, 57]:

$$f(z)=f(0)e^{\lambda\frac{f'(0)}{f(0)}}\prod_{n=1}^{+\infty}\left(1+\frac{\lambda}{k_{zn}}\right)e^{-\frac{\lambda}{k_{zn}}} \tag{A3}$$

Thus:

$$K(\lambda)=\frac{P(\lambda)}{Q(\lambda)}=\frac{P(0)e^{\lambda\frac{P'(0)}{P(0)}}\prod\limits_{n=1}^{+\infty}\left(1+\frac{\lambda}{k_{zn}}\right)e^{-\frac{\lambda}{k_{zn}}}}{Q(0)e^{\lambda\frac{Q'(0)}{Q(0)}}\prod\limits_{p=1}^{+\infty}\left(1+\frac{\lambda}{k_{zp}}\right)e^{-\frac{\lambda}{k_{zp}}}} \tag{A4a}$$

or

$$K(\lambda)=\frac{P(0)}{Q(0)}\left[\frac{e^{\lambda\frac{P'(0)}{P(0)}}}{e^{\lambda\frac{Q'(0)}{Q(0)}}}\right]\exp\left(\frac{1}{2\pi j}\int\limits_{C}\left[\ln\left(1+\frac{\lambda}{x}\right)-\frac{\lambda}{x}\right]\frac{K'(x)}{K(x)}\,dx\right) \tag{A4b}$$

Also note that if the function under study is even, then:

$$K(\lambda)=K(0)\exp\left(\frac{1}{2\pi j}\int\limits_{C}\left[\ln\left(1+\frac{\lambda}{x}\right)-\frac{\lambda}{x}\right]\frac{K'(x)}{K(x)}\,dx\right) \tag{A5}$$

In the case that a function is not meromorphic, meaning that it has branch cuts, a limiting process can be employed. Let us assume that the previous theory can be enforced as follows [40]:

$$M(\lambda)=\lim_{b\to\infty}\left[K(\lambda;b)\right] \tag{A6}$$

such that K is meromorphic, but through the limiting process it reaches M which is not meromorphic. Then it is [40]:

$$M(\lambda)=\lim_{b\to\infty}\left[K(0;b)\exp\left(\frac{1}{2\pi j}\int\limits_{C}\left[\ln\left(1+\frac{\lambda}{x}\right)-\frac{\lambda}{x}\right]\frac{K'(x;b)}{K(x;b)}\,dx\right)\right] \tag{A7a}$$

or

$$M(\lambda)=\lim_{b\to\infty}\left[K(0;b)\right]\exp\left(\frac{1}{2\pi j}\int\limits_{C}\left[\ln\left(1+\frac{\lambda}{x}\right)-\frac{\lambda}{x}\right]\frac{\lim\limits_{b\to\infty}\left[K'(x;b)\right]}{\lim\limits_{b\to\infty}\left[K(x;b)\right]}\,dx\right) \tag{A7b}$$

or

$$M(\lambda)=M(0)\exp\left(\frac{1}{2\pi j}\int\limits_{C}\left[\ln\left(1+\frac{\lambda}{x}\right)-\frac{\lambda}{x}\right]\frac{M'(x;b)}{M(x;b)}\,dx\right) \tag{A7c}$$

Comparing Eqs. (A7c) and (A5), one may observe that the exponential terms are identical, thus this expression holds irrespective if the function is meromorphic, Eq. (A5) or not, Eq. (A7). Now that Eq. (A7) has been established, let us proceed with its evaluation. In the case that the function is

not meromorphic, meaning that apart from isolated singularities, (poles), it exhibits non-isolated ones, (branch-cuts), then one may proceed as follows. The integration path that encloses all the singularities can be thought as assembled by two parts, the path that encircles all the isolated poles and the one that encircles the branch cuts:

$$\frac{M(\lambda)}{M(0)} = \exp\left(\frac{1}{2\pi j}\int\limits_{C}\left[\ln\left(1+\frac{\lambda}{x}\right)-\frac{\lambda}{x}\right]\frac{M'(x)}{M(x)}\,dx\right) \tag{A8a}$$

or

$$\begin{aligned}\frac{M(\lambda)}{M(0)} \;=\; & \exp\left(\frac{1}{2\pi j}\int\limits_{C_{\text{branch}}}\left[\ln\left(1+\frac{\lambda}{x}\right)-\frac{\lambda}{x}\right]\frac{M'(x)}{M(x)}\,dx\right) \\ & \exp\left(\frac{1}{2\pi j}\int\limits_{C_{\text{poles+roots}}}\left[\ln\left(1+\frac{\lambda}{x}\right)-\frac{\lambda}{x}\right]\frac{M'(x)}{M(x)}\,dx\right)\end{aligned} \tag{A8b}$$

or

$$\frac{M(\lambda)}{M(0)} = \exp\left(\frac{1}{2\pi j}\int\limits_{C_{\text{branch}}}\left[\ln\left(1+\frac{\lambda}{x}\right)-\frac{\lambda}{x}\right]\frac{M'(x)}{M(x)}\,dx\right)\frac{\prod\limits_{n=1}^{+\infty}\left(1+\frac{\lambda}{k_{zn}}\right)e^{-\frac{\lambda}{k_{zn}}}}{\prod\limits_{p=1}^{+\infty}\left(1+\frac{\lambda}{k_{zp}}\right)e^{-\frac{\lambda}{k_{zp}}}} \tag{A8c}$$

Note that Eq. (A8) is identical to Eq. (5) of the main text. It is important to note that for Eq. (A7), one must be able to swap the limits within the exponential integral, leading from Eq. (A7a) to Eq. (A7b). Also note that this is the case presented in the Wiener-Hopf factorization of Pathak and Kouyoumjian [40, p. 91–100], as well as in the related work of Mittra and Lee [42, p. 119, Eq. (10.16a–b)].

APPENDIX B. DEFINITION OF FUNCTIONS OF THE FACTORIZATION METHOD

A factorization procedure of characteristic equation F is employed herein. Before we proceed to the factorization procedure of a kernel-function, it is prerequisite this function converges at infinity as $\lambda^{\nu}e^{-h|\lambda|}$, with ν and h real constants and $\lambda = k_z$. Using the asymptotic expansions of Bessel and Hankel, (of second kind), functions [52, p. 364]], F behaves at infinity as $\lambda^{\nu}e^{-h|\lambda|}$ with $h = 0$, $\nu = 1$. For the branch-cut integrals of Eq. (6), these should be evaluated by substituting $x = \sqrt{k_0^2 - w^2}$ [40–45]. Since the kernel function is even, the two terms involving $\pm\lambda/x$ of the branch integral in Eq. (6) cancel each other's contribution, and only the logarithmic terms are retained according to [42]:

$$\begin{aligned}F^{\text{branches}}(\lambda) \;=\; & \exp\left[\left(q_+(\lambda)+\frac{1}{2}\ln\left(1+\frac{\lambda}{k_0}\right)\right)+\left(q_-(\lambda)+\frac{1}{2}\ln\left(1-\frac{\lambda}{k_0}\right)\right)\right] \\ =\; & \left(1-\left(\frac{\lambda}{k_0}\right)^2\right)^{1/2}\cdot\exp\left(q_+(\lambda)+q_-(\lambda)\right)\end{aligned} \tag{B1}$$

The above term $(1 \pm \frac{\lambda}{k_0})^{1/2}$ encounters the contribution at $w = 0$. The general factorized expression developed by Mittra and Lee [42, 43], reads:

$$F_{\pm}(\lambda) = \sqrt{F(0)}\left(1\pm\frac{\lambda}{k_0}\right)^{\nu_0/2}\frac{\prod_n\left(1\pm\frac{\lambda}{k_{zn}}\right)}{\prod_p\left(1\pm\frac{\lambda}{k_{zp}}\right)}\cdot e^{\frac{jk_0h}{2}-j\frac{hk_{\rho 2}}{\pi}\ln\left(\frac{\pm\lambda-k_{\rho 2}}{k_0}\right)+q_+(\lambda)+q_-(\lambda)} \tag{B2}$$

where:

$$\nu_0 = \lim_{w\to 0} wB(w) \tag{B3}$$

$$B(w) = \frac{\frac{\partial}{\partial w}F\left(\sqrt{k_0^2-w^2}\right)}{F\left(\sqrt{k_0^2-w^2}\right)} \tag{B4}$$

$$q_{\pm}(\lambda) = \int_0^{\infty} K(w)\ln\left[1\pm\frac{\lambda}{\sqrt{k_0^2-w^2}}\right]dw \tag{B5}$$

$$K(w) = \frac{h}{\pi}+\frac{1}{2\pi j}\left[B(w)+B(-w)\right] \tag{B6}$$

The opposite sign of j in Equations (B2)–(B6) is due to the $e^{+j\omega t}$ time dependence assumed herein, instead of $e^{-j\omega t}$ considered in [42, 43]. These formulas are adopted herein in order to factorize the functions $F(\lambda)$ of Eq. (5). For this purpose, functions $q_{\pm}(\lambda)$ are defined from Eq. (B5) via integration through the saddle points at $\pm\sqrt{k_0^2-w^2}$ as:

$$q_{\pm}(\lambda) = \frac{1}{2\pi j}\int_0^{\infty}\left[B(w)+B(-w)\right]\ln\left(1\pm\frac{\lambda}{\sqrt{k_0^2-w^2}}\right)dw \tag{B7}$$

Defining the variable:

$$\tau_p = \left(w^2+k_0^2\varepsilon_{r1}-k_0^2\right)^{\frac{1}{2}} \tag{B8}$$

$B(w)$ is expressed from Eq. (B4) via a symbolic computation from Mathematica [55] as

$$\begin{aligned} B(w) = {} & \left\{\left[\left[\frac{a}{2}\left(\varepsilon_{r2}\tau_p^3-\varepsilon_{r1}w^2\tau_p\right)J_0(a\tau_p)+\varepsilon_{r1}\left[\left(w^2-\tau_p^2\right)J_1(a\tau_p)+\frac{aw^2\tau_p}{2}J_2(a\tau_p)\right]\right]\cdot H_0^{(2)}(aw)\right.\right. \\ & \left.\left.+aw\tau_p^2\left(\varepsilon_{r1}-\varepsilon_{r2}\right)J_1(a\tau_p)H_1^{(2)}(aw)-\frac{a}{2}\varepsilon_{r2}\tau_p^3J_0(a\tau_p)H_2^{(2)}(aw)\right]\right\} \\ & \cdot\left[\varepsilon_{r1}w\tau_p^2J_1(a\tau_p)H_0^{(2)}(aw)-\varepsilon_{r2}\tau_p^3J_0(a\tau_p)H_1^{(2)}(aw)\right]^{-1} \end{aligned} \tag{B9}$$

The exponential term v_0 can be evaluated through Eq. (B3). This can be utilized via Mathematica [55], yielding $v_0 = 1$, as in the expression (B1). Finally, "positive $F_+(\lambda)$" and "negative $F_-(\lambda)$" are expressed as:

$$F_{\pm}(\lambda) = \sqrt{F(0)}\cdot\exp\left[\frac{1}{2\pi j}\left[\int_{\text{C-branch}}\left[\ln\left(1\pm\frac{\lambda}{x}\right)\mp\frac{\lambda}{x}\right]\frac{F'(x)}{F(x)}\,dx\right]\right]\cdot\frac{\prod_{n=1}^{+\infty}\left(1\pm\frac{\lambda}{k_{zn\pm}}\right)}{\prod_{p=1}^{+\infty}\left(1\pm\frac{\lambda}{k_{zp\pm}}\right)} \tag{B10}$$

So, F can be obtained as in the expression (8) of the main text.

APPENDIX C. NEAR FIELD AND CHARACTERISTIC EQUATION FOR DIELECTRIC ROD

For an infinitesimal, z-directed, electrical current density dipole, acting as a source and placed at (ρ', φ', z'), the field in the air-region obeys the following equation [35]:

$$\begin{bmatrix} E_{zi} \\ H_{zi} \end{bmatrix} = \frac{-j}{4\pi\omega\epsilon_1}\sum\nolimits_{m=-\infty}^{+\infty} e^{-jm(\varphi-\varphi')}\int_{-\infty}^{+\infty} dk_z e^{-jk_z(z-z')}\bar{f}_{mi}(\rho,\rho')\overleftarrow{D}_m^{(z)} \tag{C1}$$

with $\overleftarrow{D}_m^{(z)}$ defined for the current problem, as [35]:

$$\overleftarrow{D}_m^{(z)} = \begin{bmatrix} \left(\hat{z}k_1^2 - jk_z\nabla'\right)\hat{z} \\ j\omega\epsilon_1\hat{z}\left(\hat{z}\times\nabla'\right) \end{bmatrix} = \begin{bmatrix} k_1^2 - k_z^2 \\ 0 \end{bmatrix} = \begin{bmatrix} k_{\rho 1}^2 \\ 0 \end{bmatrix} \tag{C2}$$

For the external lossless air region 2, $\bar{f}_{m2}(\rho,\rho')$ gives [35, Sec. 3.1]:

$$\bar{f}_{m2}\left(\rho,\rho'\right) = H_m^{(2)}\left(k_{\rho 2}\rho\right)\bar{T}_{12}J_m\left(k_{\rho 1}\rho'\right) \tag{C3a}$$

where:

$$\bar{T}_{12} = \frac{2\omega}{\pi k_{\rho 1}^2\alpha}\bar{D}_m^{-1}\begin{bmatrix} \epsilon_1 & 0 \\ 0 & -\mu_1 \end{bmatrix} \tag{C3b}$$

$$\bar{D}_m = \left[\bar{J}_m\left(k_{\rho 1}a\right)H_m^{(2)}\left(k_{\rho 2}a\right) - \bar{H}_m^{(2)}\left(k_{\rho 2}a\right)J_m\left(k_{\rho 1}a\right)\right] \tag{C3c}$$

where $\bar{D}_m^{-1}$ is the inverse matrix of $\bar{D}_m$. Similarly, for the $i = 1$, (internal), region, $\bar{f}_{mi}(\rho,\rho')$ yields [35, Sec. 3.1]:

$$\bar{f}_{m1}\left(\rho,\rho'\right) = H_m^{(2)}\left(k_{\rho 2}\rho\right)J_m\left(k_{\rho 1}\rho'\right) + J_m\left(k_{\rho 1}\rho\right)\bar{R}_{12}J_m\left(k_{\rho 1}\rho'\right) \tag{C3d}$$

where:

$$\bar{R}_{12} = \bar{D}_m^{-1}\left[H_m^{(2)}\left(k_{\rho 1}a\right)\bar{H}_m^{(2)}\left(k_{\rho 2}a\right) - H_m^{(2)}\left(k_{\rho 2}a\right)\bar{H}_m^{(2)}\left(k_{\rho 1}a\right)\right] \tag{C3e}$$

Naming the arguments of Bessel and Hankel functions $s = k_{\rho 1}a$ and $y = k_{\rho 2}a$ the Bessel and Hankel matrices involved in Eq. (C3) are expressed as:

$$\bar{J}_m(s) = \left(k_{\rho 1}^2 a\right)^{-1}\begin{bmatrix} -j\omega\epsilon_1 sJ_m'(s) & -mk_zJ_m(s) \\ -mk_zJ_m(s) & -j\omega\mu_1 sJ_m'(s) \end{bmatrix} \tag{C4a}$$

$$\bar{H}_m^{(2)}(y) = \left(k_{\rho 2}^2 a\right)^{-1}\begin{bmatrix} -j\omega\epsilon_2 yH_m^{'(2)}(y) & -mk_zH_m^{(2)}(y) \\ -mk_zH_m^{(2)}(y) & -j\omega\mu_2 yH_m^{'(2)}(y) \end{bmatrix} \tag{C4b}$$

Substituting Eqs. (C4a)–(b) in Eq. (C3c) and after multiple algebraic manipulations, we reach expression (15), which defines the inverse D_m^{-1} function of Eq. (15) in the full text. The near field of a dielectric rod is given in the following form [35]:

$$\begin{bmatrix} E_{z2} \\ H_{z2} \end{bmatrix} = \frac{-j}{4\pi\omega\epsilon_1}\int_{-\infty}^{+\infty} dk_z e^{-jk_z(z-z')}\sum\nolimits_{m=-\infty}^{+\infty} H_m^{(2)}\left(k_{\rho 2}\rho\right)C_m \tag{C5}$$

where:

$$C_m = \begin{bmatrix} C_m^{11} \\ C_m^{12} \end{bmatrix} = e^{-jm(\varphi-\varphi')}\frac{2\omega}{\pi a}D_m^{-1}\begin{bmatrix} \epsilon_1 J_m\left(k_{\rho 1}\rho'\right) \\ 0 \end{bmatrix} \tag{C6}$$

REFERENCES

1. Poon, A. S. Y., S. Driscoll, and T. H. Meny, "Optimal frequency for wireless power transmission into dispersive tissue," *IEEE Trans. on Antennas and Propagation*, Vol. 58, No. 5, 1739–1750, May 2010.
2. Kim, S., J. Ho, and A. S. Y. Poon, "Midfield wireless powering of subwavelength autonomous devices," *Physical Review Letters*, Vol. 110, 203905, 2013.
3. Poon, A. S. Y., S. Driscoll, and T. H. Meny, "Optimal frequency in wireless power transmission for implantable devices," *Annu. Int. Conf. IEEE Eng. Med. Biol. Soc.*, 5673–5678, 2007.
4. Kim, J. and Y. Rahmat-Samii, "Implanted antennas inside a human body: Simulations, design and characterizations," *IEEE Trans. on Microwave Theory and Techniques*, Vol. 52, No. 8, 1934–1943, Aug. 2004.

5. Lin, H.-Y., M. Takahashi, K. Saito, and K. Ito, "Performance of implantable folded dipole antenna for in-body wireless communication," *IEEE Trans. on Antennas and Propagation*, Vol. 61, No. 3, 1363–1370, Jan. 2013.
6. Sasamori, T. and M. Takahashi, "Transmission mechanism of wearable device for on-body wireless communications," *IEEE Trans. on Antennas and Propagation*, Vol. 57, 936–942, Apr. 2009.
7. Ito, K. and N. Haga, "Basic characteristics of wearable antennas for body-centric wireless communications," *Loughborough Antennas & Propagation Conference*, 42–47, Nov. 8–9, 2010.
8. Akhoondzadeh-Asl, L., Y. Nechayev, and P. S. Hall, "Surface and creeping wave excitation by body-worn antennas," *Loughborough Antennas & Propagation Conference*, 48–51, Nov. 2010.
9. Liu, W., K. Vichienchom, M. Clements, S. C. DeMarco, C. Hughes, E. Mc Gucken, M. S. Humayun, E. de Juan, J. D. Weiland, and R. Greenberg, "A neuro-stimulus chip with telemetry unit for retinal prosthetic device," *IEEE J. Solid-State Circuits*, Vol. 35, No. 10, 1487–1497, Oct. 2000.
10. Collin, R. E. and F. Zucker, *Antenna Theory. Part I & II*, McGraw Hill, 1969.
11. Tamir, T. and A. A. Oliner, "Guided complex waves. Part I: Fields at an interface," *Proc. IEEE*, Vol. 110, 310–324, Feb. 1963.
12. Tamir, T. and A. A. Oliner, "Guided complex waves. Part II: Relation to radiation patterns," *Proc. IEE*, Vol. 110, 325–334, Feb. 1963.
13. Yaghjian, A. D. and R. A. Shore, "General properties of complex waves," *2012 International Conference on Electromagnetics in Advanced Applications*, 2012.
14. Shigesawa, H. and M. Tsuji, "The nature of spectral gap between bound and leaky solutions with dielectric loss is present in printed-circuit lines," *Radio Science*, Vol. 28, No. 6, 1235–1243, 1993.
15. Neve, M. J. and R. Paknys, "A technique for approximating the location of surface and leaky wave poles for a lossy dielectric slab," *IEEE Trans. on Antennas and Propagation*, Vol. 51, No. 1, 115–120, 2006.
16. Kamel, A. H. and A. S. Omar, "Effect of losses on the spectral transition of modal poles between the improper and proper riemann sheets," *IEEE MTT-S International Microwave Symposium Digest*, 715–718, 2001.
17. Frezza, F. and N. Tedeschi, "Electromagnetic inhomogeneous waves at planar boundaries: Tutorial," *Journal of Optical Society of America*, Vol. 32, 1485–1501, 2015.
18. Frezza, F. and N. Tedeschi, "Deeply penetrating waves in lossy media," *Optics Letters*, Vol. 37, No. 13, 2616–2618, 2012.
19. Baccarelli, P., F. Frezza, P. Simeoni, and N. Tedeschi, "An analytical study of electromagnetic deep penetration conditions and implications in lossy media through inhomogeneous waves," *MDPI Materials*, Vol. 11, No. 4, 1595, 2018.
20. Frezza, F. and N. Tedeschi, "On the electromagnetic power transmission between two lossy media: Discussion," *Journal of Optical Society of America*, Vol. 29, No. 11, 2012.
21. Snyder, A. W., "Continuous mode spectrum of a circular dielectric rod," *IEEE Trans. on Microwave Theory and Techniques*, Vol. 19, No. 8, 720–727, 1971.
22. Snyder, A. W. and D. J. Mitchell, "Leaky mode analysis of circular optical waveguides," *Optoelectronics*, 287–296, 1974.
23. Ip, A. and D. R. Jackson, "Radiation from cylindrical leaky waves," *IEEE Trans. on Antennas and Propagation*, Vol. 38, No. 4, 482–488, 1990.
24. Lovat, G., P. Bughignoli, and D. R. Jackson, "Fundamental properties and optomization of broadside radiation from uniform leaky-wave antennas," *IEEE Trans. on Antennas and Propagation*, Vol. 54, No. 5, 1442–1452, May 2006.
25. Ostner, H., J. Detlefsen, and D. R. Jackson, "Radiation from one-dimensional leaky-wave antennas," *IEEE Trans. on Antennas and Propagation*, Vol. 43, No. 4, 331–339, Apr. 1995.
26. Wait, J. R., *Electromagnetic Radiation from Cylindrical Structures*, Pergamon, New York, USA, 1959.
27. Snitzer, E., "Cylindrical dielectric waveguide modes," *Journal of Optical Society of America*, Vol. 51, No. 5, 491–498, May 1961.

28. Shevchenko, V. V., "On the behavior of wave numbers beyond the critical value for waves in dielectric waveguides," *Radiophysics and Quantum Electronics*, Vol. 15, 194–200, 1972.
29. Shevchenko, V. V., "The expansion of the fields of open waveguides in proper and improper modes," *Radiophysics and Quantum Electronics*, 972–977, 1971.
30. Shevchenko, V. V., "Electromagnetic waves in an isotropic stratified plasma waveguide," *Izvestiya VUZ. Radiofizika*, Vol. 9, No. 1, 110–125, 1966.
31. Singh, M., B. Ghosh, and K. Sarabandi, "Excitation of space wave, leaky wave and creeping waves in cylindrical media," *IEEE Trans. on Antennas and Propagation*, Vol. 66, No. 12, 7100–7110, 2018.
32. Ufimtsev, P. Y., R. T. Ling, and J. D. Scholler, "Transformation of surface waves in homogeneous absorbing layers," *IEEE Trans. on Antennas and Propagation*, 214–222, Feb. 2000.
33. Wang, Z., H. Jiang, and H. Chen, *CMOS IC Design for Wireless Medical and Health Care*, 1st Edition, Springer, 2014.
34. Ishimaru, A., *Electromagnetic Wave Propagation, Radiation and Scattering*, 2nd Edition, IEEE Press Series on Electromagnetic Wave Theory, Wiley, 2017.
35. Chew, W. C., *Waves and Fields in Inhomogeneous Media*, 1st Edition, IEEE on Electromagnetic Wave Theory, 1995.
36. Harrington, R. F., *Time Harmonic Electromagnetic Fields*, 2nd Edition, IEEE on Electromagnetic Wave Theory, 2001.
37. Fuscaldo, W., "Advanced radiation systems based on leaky waves and nondiffracting waves," Ph.D Thesis, 2017.
38. Felsen, L. B. and N. Marcuvitz, *Radiation and Scattering of Waves*, 2nd Edition, IEEE on Electromagnetic Wave Theory, 1994.
39. Rojas, R., "Comparison between two asymptotic methods," *IEEE Trans. on Antennas and Propagation*, Vol. 35, No. 12, 1489–1492, 1987.
40. Pathak, P. H. and R. G. Kouyoumjian, "TM surface wave diffraction by a truncated dielectric slab recessed in a perfectly conducting surface," *NASA Contractor Report*, May 1974.
41. Bates, C. P. and R. Mittra, "A technique for solving certain Wiener-Hopf type boundary value problems," *Antenna Laboratory Report*, No. 66-4, 1966.
42. Mittra, R. and S. W. Lee, *Analytical Techniques in the Theory of Guided Waves*, The Mac Millan Company, New York, 1971.
43. Bates, C. P. and R. Mittra, "A factorization procedure for Wiener-Hopf kernels," *IEEE Trans. on Antennas and Propagation*, Vol. 17, No. 1, 102–103, Jan. 1969.
44. Fikioris, J. G., J. L. Tsalamengas, and N. K. Uzunoglu, "Analysis of a semi-infinite microstrip patch loaded with a ferrite substrate," *Electromagnetics*, Vol. 3, 271–288, 1983.
45. Mitsalas, X. M., T. Kaifas, and G. Kyriacou, "Wiener-Hopf analysis of planar canonical structures loaded with longitudinally magnetized plasma biased normally to the extraordinary wave propagation: Near and far field," *Progress In Electromagnetics Research B*, Vol. 88, 119–149, 2020.
46. Gennarelli, C. and L. Palumbo, "A uniform asymptotic expansion of a typical diffraction integral with many coalescing simple pole singularities and a first order saddle point," *IEEE Trans. on Antennas and Propagation*, Vol. 32, No. 10, 1122–1124, 1984.
47. Hejase, H. A. N., "On the use of Davidenko's method in complex root search," *IEEE Trans. on Microwave Theory and Techniques*, Vol. 41, No. 1, 141–143, Jan. 1993.
48. Talisa, S. H., "Application of Davidenko's method to the solution of dispersion relations in lossy waveguiding systems," *IEEE Trans. on Microwave Theory and Techniques*, Vol. 33, No. 10, 967–971, Oct. 1985.
49. Yang, S. and J.-M. Song, "Analysis of guided and leaky TM_{0n} and TE_{0n} modes in circular dielectric waveguide," *Progress In Electromagnetics Research B*, Vol. 66, 143–156, 2016.
50. Senior, T. B. A. and J. L. Volakis, *Approximate Boundary Conditions in Electromagnetics*, IEE Electromagnetic Wave Series, 1995.

51. Volakis, J. L. and M. I. Herman, "A uniform asymptotic evaluation of integrals," *Proceedings of IEEE*, Vol. 74, No. 7, 1043–1044, 1986.
52. Abramowitz, M. and I. A. Stegun, *Handbook of Mathematical Functions with Formulas, Graphs and Mathematical Tables*, Dover Books on Mathematics, 1965.
53. Daniele, V. G. and R. S. Zich, *The Wiener-Hopf Method in Electromagnetics*, SciTech Publishing, 2014.
54. Pozar, D. M., *Microwave Engineering*, 3rd Edition, J. Wiley, 2007.
55. Wolfram Mathematica 11.0.1.
56. Sammut, R. A., "The theory of unbound modes on circular dielectric waveguides," Ph.D. Thesis, 1975.
57. Titchmarsh, E. C., *Theory of Functions*, 2nd Edition, Oxford University Press, 1939.